The cell-cell adhesion protein JAM3 determines nuclear deformability by regulating microtubule organization.

Mar Arias-Garcia[1], Rebecca Rickman[1], Julia Sero[1], Yinyin Yuan [2,3], Chris Bakal [1,2,3]

[1] Dynamical Cell Systems Team. Chester Beatty Laboratories, The Institute of Cancer Research, 237 Fulham Road, London UK, SW3 6JB

[2] Computational Pathology and Integrative Genomics Team. The Institute of Cancer Research, 15 Cotswold Road, Sutton, SM2 5NG

[3] Address correspondence to **yinyin.yuan@icr.ac.uk** and **chris.bakal@icr.ac.uk**

Abstract

The shape, size, and architecture of the nucleus determines the output of transcriptional programmes. As such, the ability of the nucleus to resist deformation and maintain its shape is essential for homeostasis. Conversely, changes in nuclear shape can alter transcription and cell state. The ability of cells to deform their nuclei is also essential for cells to invade confined spaces. But how cells set the extent of nuclear deformability in response to their environment is unclear. Here we show that the cell-cell adhesion protein JAM3 regulates nuclear shape. In epithelial cells, JAM3 is required for maintenance of nuclear shape by organizing microtubule polymers and promoting LMNA stabilization in the nuclear membrane. Depletion of JAM3 in normal epithelial cells leads to dysmorphic nuclei, which leads to differentiation into a mesenchymal-like state. Inhibiting the actions of kinesins in JAM3 depleted cells restores nuclear morphology and prevents differentiation into the mesenchymal-like state. Critically, JAM3 expression is predictive of disease progression. Thus JAM3 is a molecule which allows cells to control cell fates in response to the presence of neighbouring cells by tuning the extent of nuclear deformability.

Introduction

Nuclear shape, size and architecture define the biophysics of key cellular processes such as transcription, replication, mRNA export, and DNA damage repair[1-4]. But nuclei are malleable viscoelastic structures[5, 6] that are frequently being stretched, strained, and compressed both by extracellular forces[7], and the internal cytoskeleton[8-12]. Mechanisms have evolved to maintain nuclear shape and genome organization when cells are exposed to these forces[13]. Indeed, dysregulation of nuclear shape is coincident with numerous diseases including: muscular dystrophies, heart disease, and aging disorders such as progeria[14-18]. Thus in many cells, maintaining nuclear shape is essential for homeostasis.

But while clearly maintenance of nuclear shape, size, and genome organization is essential for cellular homeostasis, transcriptional programmes that alter cell fate can be engaged by altering nuclear morphology and architecture[1, 5, 19-22]. For example, nuclei undergo extensive shape changes that drive differentiation during development[23]. One means by which alteration in nuclear shape affects transcription is by affecting the nuclear translocation dynamics of transcription factors such as YAP/TAZ and NF-κB[24, 25]. Thus while in some cell types nuclear shape and genome organization are robust to deformation, in other cell types the nucleus is highly deformable.

The importance of maintaining nuclear shape for cell, tissue, and organism homeostasis is highlighted by the fact that changes in nuclear morphology and genome organization are associated with cancer[4, 26]. For example, nuclear rupture is frequently an oncogenic event[27, 28]. Indeed, pathologists have used nuclear shape as a diagnostic for over a century[29]. Irregular nuclear shapes and sizes are hallmarks of cancer cells; whereas smooth, roundish forms are characteristic of normal cells[30]. Both the cause and consequences of these nuclear shape deformations in cancer progression are not clear. In some cancer cells, a highly deformable nucleus is necessary to squeeze through small pores (<10 microns) in 3D environments during confined migration[31, 32]. Dysregulation in nuclear morphogenesis is also linked to genome instability[33], alterations in the dynamics of DNA damage repair[4, 34, 35], and the activation of pro-inflammatory pathways[24, 27] – all of which can contribute to tumorigenesis and metastasis.

Polymers of actin, tubulin, and vimentin appear to have unique roles in maintaining nuclear shape when cells are exposed to different forces of varying magnitudes[11, 19, 36, 37]. In epithelial cells, the anchoring of microtubule (MT) minus-ends at cell-cell adhesion complexes results in the stabilization, nucleation, and polymerization of MTs along the apicobasal axis[38-42], and the

capture of plus-end MTs by nuclear bound SYNE-4, a scaffolding protein that is part of SUN-KASH complexes which interact with plus-end directed Kinesin-1 MT-bound motors[19]. Thus MTs which bridge cell-cell adhesions and the nucleus can act to promote nuclear mechanical stability and decrease the effective deformability of the nucleus[6, 11, 43].

But the cytoskeleton can also itself act to deform the nucleus, and in turn regulate cell behaviour and fate; perhaps the best example of which is the separation of chromatin during cell division by the mitotic spindle[44]. The cytoskeleton has a role in shaping the nucleus as migrating cells pass through confined spaces during development and disease[10, 45-48]. Finally, the cytoskeleton deforms to nucleus to promote differentiation[49, 50], and DNA repair[51].

In addition to the cytoskeleton, another key factor in determining nuclear deformability is the composition of the nuclear lamina – which is comprised primarily of LMNA and LMNB proteins. The LMNA:LMBA ratio determines the viscoelasticity of the nucleus. LMNA scales with tissue rigidity, and increased levels protect against deformation; as evidenced by observations that the nuclei of the same cell type on matrices of low stiffness are more “wrinkled” than those on high stiffness[52]. LMNB levels set nuclear viscosity, where nuclei with high LMNB levels are capable of maintaining shapes regardless of their pliability[52]. Importantly, the LMNA:LMNB ratio is rate limiting for the invasion of cells into confined spaces, and reduction in LMNA allows migration in three dimensional matrices[53]. How LMNA and LMNB levels, and the LMNA:LMNB ratio, are regulated in largely unclear. One important means of regulating LMNA levels that are incorporated is via phosphorylation of LMNA[54].

But how the deformability of the nucleus is dynamically tuned by controlling the cytoskeleton and the LMNA:LMNBA ratio is unclear. Because cancer cells have dysregulated nuclear shapes, we reasoned gene expression changes in these cells may point to mechanisms as to how cells either protect or deform nuclei. Thus, we first used an integrative approach to identify mRNAs whose expression is associated with nuclear shape changes in breast cancer patients. Our analysis revealed that the gene encoding the cell-cell adhesion component JAM3 is a tumour suppressor that maintains nuclear shape *in vivo*. We show that in normal breast epithelial cells, depletion of JAM3 results in a change in MT organization that leads to alterations in nuclear shape. MT-mediated alterations in nuclear shape leads to increased YAP/TAZ activation, remodelling of the ECM, changes in the organization of the nuclear envelope, and increased ability of cells to invade three-dimensional matrices. Uncoupling MTs and the MT-bound kinesin Kinesin-1 in JAM3 depleted cells restores nuclear shape, reverses invasive phenotypes, and decreases YAP/TAZ nuclear translocation. Taken together these data show that the material properties of the nucleus in epithelial cells are determined by cell-

cell adhesion complexes that control MT organization. Moreover, the ability of cells to dynamically alter these material properties dictates cell fates.

Results

Hybrid network topological analysis of nuclear morphology and gene expression

Dysmorphic nuclei are a hallmark of cancer cells[29]. Thus we identified genes whose levels correlated with changes in nuclear shape in 1,000 invasive human breast tumours[55]. We described the shape of single cancer cell nuclei, and the morphological heterogeneity of tumour cell nuclei *in vivo* by quantifying six shape features of tumour cell nuclei, but not the nuclei of lymphocytes or stromal cells, in haematoxylin and eosin (H&E) stained sections (Supplemental Table 1; Figure 1A). For all features, a higher value indicates more irregular/elongated morphology, whilst a low value indicates a regular/round morphology. On average, there were 6×10^4 cancer cells in the H&E sections in each tumour, and we used three statistics – median, standard deviation (sd), and skewness – to characterize the distribution of nuclear shape features in a tumour (Figure 1A). In total, 18 nuclear morphology scores were obtained for each tumour. Batch effects arising from different hospital sites and different staining and processing procedures were corrected for (Methods).

To identify cancer-driven molecular changes, we first identified the top 1,000 cis-driven genes based on association between DNA copy number alterations and mRNA expression across the 1,000 invasive breast cancers[55]. We then determined how the expression and copy number of these genes correlated with nuclear morphology and cell-to-cell variability in nuclear shape. The strongest gene expression-nuclear shape associations were used to construct a hybrid network ($q<0.01$ of false discovery rate (FDR); Spearman correlation corrected), with the core network module connecting 6 morphological scores and 38 gene expression probes representing 32 unique genes ($q<0.005$, Figure 1B). Nodes represent morphological scores or genes, and edges denote significant correlations. Given these genes were pre-selected based on their copy-number and gene expression profiles, this network effectively links DNA copy number, gene expression, and nuclear morphology.

Topology analysis of this network revealed that a morphological score “median I1” was positioned as the best-connected network hub (Methods). This feature describes rotational stability given the shape of an object. Intuitively, an object with irregular shape has a high I1 value. Cells and tumour tissues with different median I1 values are shown in Figures 1C and 1D. We henceforth refer to this morphological score as the Cancer Nuclear Instability index (CNI). Notably, “instability” here refers to a morphological property, as opposed to genomic instability. Well-differentiated epithelial-like cells have high CNI, whereas low CNI cells have

abnormally-shaped nuclei (Figure 1D). Consistent with the idea that low CNI is a marker of cancer progression and aggressiveness, this score has a strong negative association with the mRNA levels of genes previously implicated in breast tumorigenesis including MCM4[56], MCM10[57], FOXM1[58], CCNE2[59], and MASTL[60] (Figure 1B). In addition, heterogeneity measures including standard deviation and skewness of morphology scores were also identified in this core network module; indicating that gene expression in single cells correlates with the exent of nuclear morphology heterogeneity in breast tumour cells *in vivo*. Thus both median changes in nuclear morphology, as well as cell-to-cell variability in nuclear morphology are coupled to transcriptional upregulation of known oncogenes.

JAM3 mRNA expression correlates with nuclear morphology in breast cancer

To identify genes that are positively associated with CNI, and thus are putative tumour suppressors, we performed correlation analysis of CNI and genome-wide mRNA expression revealing 735 significant correlations (FDR correction q<0.01). CNI positively correlated with the mRNA expression of a number of genes encoding components of cell-cell adhesions, among which is JAM3 (Junctional Adhesion Molecule 3) whose mRNA was highly correlated with CNI (correlation=0.37, q-value 2.9×10^{-6}) (Figure 2A). JAM3 mRNA expression was strongly cis-driven (FDR corrected Spearman correlation among genome-wide associations between copy number and expression q-value=1×10^{-7}), and was predominately lost in breast cancer (13% copy-number loss and only 0.8% gains; Figure 2B). The expression of JAM3 mRNA was lower in more aggressive Basal, HER2, and Luminal B subtypes compared to the less aggressive Luminal A subtype and “normal” subtypes (Figure 2C). JAM3 mRNA expression differed significantly in the 10 subtypes, among which “IntClust4” and “IntClust10” subtypes had the highest and lowest levels of JAM3 mRNA respectively (Figure 2D). IntClust4, which had high JAM3 mRNA expression, is the ‘CNA-devoid’ (no copy number alteration) group with favourable prognosis and a significant proportion of cases presented with extensive lymphocytic infiltration[55]. IntClust10, which had the lowest JAM3 mRNA expression, included the majority of Basal-like samples with high genomic instability. JAM3 mRNA expression was also lower in invasive ductal carcinoma (IDC) compared to less aggressive invasive lobular carcinoma (ILC) histology type (Figure 2F). The expression of JAM3 mRNA was also negatively correlated with tumour grade (Figure 2F). Thus JAM3 expression scales with cancer aggressiveness. Because JAM3 levels also correlate with changes in nuclear shape, we predicted that JAM3 deficiency drives oncogenesis by changing nuclear shape.

JAM3 regulates microtubule and nuclear morphogenesis

To investigate the role of JAM3 in regulating nuclear shape, we used quantitative single cell morphological analysis[61] to assess how depletion of JAM3 affected the cell and nuclear shape

of non-transformed MCF10A mammary epithelial cells. To this end, we used single or pooled small interfering RNAs (siRNAs) that effectively reduced JAM3 mRNA and/or protein. Two different pools (siGENOME or "siG", and On-Target Plus or "OTP") reduced JAM3 mRNA levels by 95 percent, and all individual siRNAs that constituted each pool reduced JAM3 mRNA levels between 75 and 97 percent (Figure S1A). Consistent with previous reports[62-65], JAM3 protein is localized to the cell-cell junctions of MCF10A non-transformed epithelial cells, and the siG pool reduced JAM3 to virtually undetectable levels as judged by immunofluorescence (Figure 3A). The siG and OTP pools effectively depleted JAM3 protein in MCF10A as judged by Western blotting (Figure S1B). Although both siRNA pools and all individual siRNAs from each pool are highly effective at reducing JAM3 mRNA, for the majority of our experiments we used the siG pool and/or a single siRNA, OTP5, to deplete JAM3.

Depletion of JAM3 by different siRNAs did not disrupt the ability of MCF10As to form cell-cell adhesions, as shown by the overall morphology of highly confluent cultures, and the accumulation of β-catenin at cell-cell borders. However, the β-catenin positive cell-cell junctions in JAM3 knockdown cells had altered morphology compared to mock treated junctions and appeared "jagged" (Figure 3A). But in contrast to the relatively mild effects on cell-cell adhesion, depletion of JAM3 by siRNA resulted in the dramatic reorganization of MT structures. Whereas the MTs of wild-type cells were organized into parallel filaments that span the long axis of the cell, and loosely grouped in the perinuclear region (Figure 3B arrows); the MTs of JAM3 depleted cells were consistently organized into radial arrays with highly focused microtubule organizing centres (MTOC) (Figure 3B chevrons). Differences in MT organization between wild-type and JAM3 depleted cells were quantified by measuring the intensity of MTs in the perinuclear region, and JAM3 depleted cells had significant higher perinuclear MT intensity (Figure 3C). These data suggest that JAM3 is not essential for the formation of cell-cell adhesions and regulates MT morphogenesis.

JAM3 depletion in MCF10A cells also resulted in striking changes in nuclear morphology. The vast majority of nuclei of normal MCF10A cells were shaped like smooth ovals. In contrast, the nuclei of JAM3 depleted cells had highly irregular, banana-like shapes, and a proportion had large holes in the nuclei (Figure 3B asterisks). We termed the nuclei with large holes "donut" nuclei. Using a linear classifier we automatically identified donut nuclei in cellular populations (Methods). Normal cell populations had ~1% of nuclei that could be classified as donuts, but JAM3 depletion increased the proportion of donut nuclei population to ~10-20% (Figure 3D). Inhibition of JAM3 by 3/4 individual siRNAs from the siG pool, or 2/4 siRNAs from the OTP pool (Figure S1C), led to significant increases in donut nuclei. Because these individual siRNAs target different sequences this eliminates the possibility this phenotype can

be attributed to off-target effects. The MTOC of JAM3 depleted cells was almost always positioned in the hole of nuclear donuts, or at deepest point of invagination in banana nuclei (Figure 3C, arrow). Knockdown of JAM3 in other normal epithelial cell types, such as Retinal Pigmented Epithelial (RPE-1) cells, had identical effects on nuclear morphology (Figures S1D and S1E). Notably, depletion of JAM3 had little effect on the organization of the actin cytoskeleton, especially near the nucleus (Figure S1F); and the levels of actin near the nucleus were identical between control and JAM3 depleted cells, and JAM3 depletion resulted in a small decrease in the number of actin filaments (Figure 1G). Taken together, these data suggest that JAM3 plays an important role in normal epithelial cell morphogenesis by regulating MT organization and nuclear shape.

JAM3 depleted cell gain the ability to invade

We hypothesized that a change in nuclear shape following JAM3 depletion may be a characteristic of increased nuclear deformability and/or a change into a mesenchymal-like state. Indeed bundled radial MT arrays in JAM3 depleted cells are characteristic of fibroblast or mesenchymal cells, and unlike the thin parallel filaments of non-centrosomal MT arrays found in epithelial cells[41]. To test this idea, we asked whether JAM3 depletion resulted in non-invasive MCF10A cells gaining the ability to invade 3D collagen matrices where nuclei are compressed as they move through pores in the matrix - a characteristic of mesenchymal cells. Whereas normal MCF10A cells do not invade collagen matrices, JAM3 depleted cells invaded the gels to heights of 60 μm in 24 hr (Figure 3E). Collagen invasion was dependent on Matrix Metalloproteinases (MMPs; Figure 3F). The mesenchymal-like phenotype following JAM3 loss was confirmed by the observation that JAM3 deficient cells upregulate pro-mesenchymal mRNAs including Fibronectin-1 (FN), ITGA5, MMP3, BMP1, and MAP1B, and downregulate pro-epithelial mRNAs such as KRT14 and KRT19 (Figure 3G). We confirmed upregulation of individual mRNAs by qPCR (Figure S1F). Thus JAM3 depletion results in MCF10A epithelial cells differentiating into an invasive mesenchymal-like state.

To explore whether changes in nuclear and MT morphology occur during differentiation into mesenchymal-like states induced by other stimuli, we treated MCF10A cells for 48 hrs with TGF-β[66]. Indeed TGF-β treatment led to significantly increases in the sub-population of cells with low nuclear roundness to a similar extent as JAM3 depletion alone. Addition of TGF-β to JAM3 depleted cells nearly doubled the population of cells with low nuclear roundness (Supplemental Figure S2A). Thus changes in nuclear shape, from round to deformed, are characteristic of differentiation into a mesenchymal-like state.

To assess MT orientation in JAM3 depleted cells, we also quantified the distribution of the plus-end binding protein EB1 following JAM3 depletion +/- TGF-β stimulation. In control MCF10A cells EB1 was predominantly distributed as small parallel filaments in the cytoplasm. However, in JAM3 depleted cells, TGF-β treated cells, or TGF-β treated JAM3 depleted cells, EB1 was primarily localized to the cell periphery and the leading edge (Supplemental Figure S2B,C). These data support classical observations that epithelial versus mesenchymal-like cells have differences in MT organization[41].

JAM3 is required for the morphogenesis of epithelial tissues

To assess the role of JAM3 in promoting epithelial morphogenesis, we investigated the ability of JAM3-deficient MCF10A cells to form 3D acini structures in solid matrices in mixtures of Matrigel and Collagen-I (Col-I; Methods). After four days in 3D matrices, normal MCF10A cells formed round structures with a well-organized thin outer layer of laminin-5 (Figure 4A,B). In contrast, JAM3 depletion decreased both the total number of acini, and the number cells in each organoid structure (Figure 4A,B). Unlike wild-type acini (Figure S3, arrows) JAM3-depleted acini also frequently formed large protrusions (Figure S3, chevrons), that were F-actin rich (Figure 4A, arrows). The laminin-5 basement membrane in JAM3-depleted acini was virtually non-existent compared to wild-type, but FN was organised into large bundles that encapsulated the acini (Figure 4A, chevrons). Over eight days, JAM3-depleted acini developed into irregularly shaped bodies which often fused into larger multi-acinar structures (Figure 4C,D). These results demonstrate JAM3 is essential for mammary acini morphogenesis in 3D.

JAM3 suppresses the activity of YAP and TAZ

We hypothesized that because JAM3 depletion alters microtubule and nuclear morphogenesis, which coincides with differentiation into a mesenchymal-like state, this may result in nuclear translocation and activation of the YAP and/or TAZ transcriptional co-activators. Both YAP and TAZ are structurally related proteins, with only partially overlapping functions, that translocate from the cytoplasm to nucleus in response to forces on the nucleus[25, 67, 68], and regulate the transcription of genes that results in changes in cell shape, promote migration, proliferation, and invasion[69-71]. In wild-type MCF10A cells cultured at medium to high densities, both YAP and TAZ are predominantly localized to the cytoplasm as determined by immunofluorescence staining (Figure 5A,B) using antibodies specific to these proteins (Figure S4A-C). However, both YAP and TAZ localize to the nucleus after downregulation of JAM3 by RNAi as determined by immunofluorescence (Figure 5A,B). To confirm that JAM3 depletion results in a change in the subcellular localization of YAP and TAZ,

we performed biochemical fractionation of mock-treated and JAM3 depleted cells, and quantified the levels of YAP and TAZ in each fraction by Western blotting. Indeed, JAM3 depletion resulted in a significant accumulation of both YAP and TAZ protein in the nuclear fraction (Figure 5C), and depletion of YAP and TAZ from membrane fractions (Figure 5D). JAM3 depletion also resulted in YAP and TAZ activation as well as increased nuclear translocation as CTGF mRNA, a canonical target of YAP/TAZ mediated transcription[72] is also upregulated following JAM3 depletion (Figure 5E). Thus decreases in JAM3 and changes in nuclear shape correlated with increased YAP/TAZ activity.

We next determined if YAP and/or TAZ are required for the invasive phenotypes of JAM3-depleted cells. Following JAM3 depletion, the mRNA levels of genes encoding ECM proteins such as Col-I and FN are increased (Figure 1F), and we also observe JAM3 depletion increases the protein levels of Col-I (Figure S5A) or FN (Figure S5B) compared to control cells. Co-depletion of JAM3 with TAZ, but not YAP restored Col-I production to control levels (Figure S5A). Conversely, co-depletion of JAM3 with YAP, but not TAZ, restored levels of FN to control levels (Figure S5B,C). These phenotypes are specific to YAP and TAZ depletion because YAP and TAZ RNAi do not deplete each other (Figure S4A, B). Thus, changes in the ECM following JAM3 depletion are due to TAZ-dependent production of Col-I, and YAP-dependent production of FN.

To assess whether YAP and/or TAZ activity are responsible for the protrusive structures we observed to form in JAM3-deficient 3D acini (Figure 4A), we knocked down YAP or TAZ in control or JAM3-deficient MCF10A organoids. Depletion of neither YAP nor TAZ alone prevented acini formation (Figure 6A). But while co-depletion of JAM3 and YAP1 resulted in acini with multiple actin-rich protrusive structures similar to acini depleted of JAM3 alone (Figure 6A,B), co-depletion of TAZ with JAM3 completely abrogated the formation of actin-rich invasive structures (Figure 6A,B). Thus TAZ, but not YAP1, mediated transcriptional regulation is essential for the generation of protrusive structures made by abnormal acini following JAM3 depletion.

Uncoupling the nucleus from MTs cytoskeleton rescues the phenotypes of JAM3 depletion

To determine if cytoskeletal reorganization was responsible for nuclear deformation in JAM3 deficient cells we systematically depleted components of complexes which mediate the coupling of either the actin or MT cytoskeletons with the nucleus. In epithelial cells, both the actin and MT cytoskeletons are directly coupled to the nucleus via SUN-KASH complexes[19]. SUN1 and SUN2 are ubiquitous members of these complexes that are embedded into the nuclear membrane, and Nesprin/SYNE proteins serve as adaptors which link SUN1/2 to

specific cytoskeletal components. SYNE1 and SYNE couple the SUN complexes to F-actin filaments, and SYNE3 couples SUN complexes to intermediate filaments[73, 74]. The Kinesin-1 heavy chain KIF5B interacts with SYNE4 to couple MTs to the nucleus[75, 76]. We systematically depleted all known SUN-KASH components individually, as well as SYNE4 and KIF5B in combination, in JAM3-depleted cells to determine if uncoupling the nucleus from the cytoskeleton rescued nuclear and MT phenotypes. Only co-depletion of JAM3, SYNE4, and KIF5B (hereafter referred to as the "triple" knockdown) led to a complete reversion of the abnormal nuclear shape (Figure 7A) and MT reorganization (Figure 7B) observed in JAM3 deficient cells alone. Specifically, donut nuclei were clearly observed in all conditions except the triple knockdown (Figure 7C, chevrons. Triple knockdown in green box). Although the MTs in triple knockdown cells were still organized as radial arrays with a clear central MTOC, the concentration of polymerized MTs was significantly decreased. Co-depletion of JAM3 with SYNE1, SYNE2, or SYNE3 did not rescue the phenotypes of JAM3 depletion suggesting that actin or intermediate filaments do not play a role in nuclear deformation in JAM3 depleted cells. These results support the idea that disrupting the complexes that bridge the MTs and the nucleus by depleting SYNE4 and KIF5B can prevent MTs from deforming the nucleus in JAM3 depleted cells.

To determine if the rescue of nuclear shape phenotypes in JAM3 depleted cells following depletion of SYNE4 and KIF5B also reversed the upregulation of YAP/TAZ and the engagement of pro-invasive programmes, we measured 3D invasion, CTGF expression, and YAP or TAZ nuclear translocation in: 1) normal cells; 2) cells depleted of JAM3, KIF5B, or SYNE-4 alone; 3) cells co-depleted of JAM3 and KIF5B or SYNE-4; and 4) cells co-depleted of JAM3, KIF5B, and SYNE-4 (triple knockdown). Whereas depletion of JAM3 alone, or co-depletion of JAM3 and KIF5B or SYNE-4, led to increased invasion, the triple knockdown cells did not invade (Figure 7D). Notably, co-depletion of the actin binding protein SYNE-2 and JAM3 did not prevent invasion (Figure 7E). Depletion of both SYNE-4 and KIF5B in combination with JAM3 also reduced CTGF mRNA expression (Figure 7F), nuclear YAP (Figure 7G) and nuclear TAZ (Figure 7H) compared to JAM3 knockdown alone as determined by immunofluorescence of endogenous YAP and TA localization (Figure 7I). The ability of triple RNAi to restore YAP and TAZ nuclear levels to those of wild-type was confirmed by Western blotting for YAP and TAZ in lysates following subcellular fractionation (Figure 7J,K). Thus, the function of both KIF5B and SYNE-4 are required for phenotypes, in particular the increased invasiveness, associated with mesenchymal-like cells following depletion of JAM3. The data support a model where depletion of JAM3 results in changes in MT organization that cause nuclear deformation, YAP/TAZ activation, and entry into an invasive, mesenchymal-like state. But disrupting the complexes that couple the MTs to the nucleus prevents: nuclear

deformation; the activation transcription factors such as YAP/TAZ; and the ability of JAM3 depleted cells to invade 3D matrices.

Loss of JAM3 disrupts the LMNA:LMNB ratio

The defects in nuclear morphogenesis following JAM3 depletion were highly reminiscent of nuclear morphology defects observed in cells with dysfunctional LMNA, such as progeric cells[18]. The viscoelastic properties of the nucleus are partly determined by the levels of both LMNA and LMNB, although LMNA levels have been observed to vary to much greater extents than LMNB, suggesting that the LMNA:LMNB ratio is a key factor in determining nuclear viscoelasticity[52, 77]. We speculated that the altered nuclear shapes in JAM3 depleted cells could also be in part due to changes in LMNA and/or LMNB levels in the nuclear lamina. Using siRNAs that specifically depleted LMNA or LMNAB protein (Figure S6A,B) and mRNA (Figure S6B) we observed that knockdown of LMNA, but not LMNB, increased the percentage of misshapen nuclei in the population, and that of the number of donut shaped nuclei in particular (Figure 8A). But while combined depletion of LMNA and JAM3 also led to a marked increase in the percentage of misshapen nuclei in the population, the nuclei of JAM3 and LMNB deficient cells were the same shape as wild-type nuclei (Figure 8B chevrons). Because reduction of LMNB, but not LMNA, restores the nuclear morphology defects in JAM3 cells, we propose the effects on JAM3 depletion are at least in part due to decreased level of LMNA relative to LMNB, and thus the viscoelasticity of the nucleus.

We next sought to determine whether JAM3 regulates LMNA and/or LMNB levels or localization in a manner that is dependent on SYNE4 and KIF5B. As expected LMNA and LMNB are primarily localized to the entire nucleus as assessed by immunofluorescence (Figure 8C). To assess the amount of LMNA and LMNB in the nuclear lamina, we compared the amount of protein localized to the outer ring region of the nucleus compared to the inner region (outer:inner ratio). (Figure 8D,E; Figure S5B). Depletion of JAM3 affected both the outer:inner nuclear ratio of LMNA (Figure 8C,D) and LMNB (Figure 8C,E). Combined depletion of SYNE4 and KIF5B in the background of JAM3 depletion (the “triple” knockdown) restored the levels of LMNA (Figure 8D) but not LMNB (Figure 8E) in the nuclear lamina. The alterations in LMNA and LMNB localization following JAM3 depletion were not due to decreases in either LMNA or LMNB mRNA levels (Figure S6C), or the ratio of LMNA:LMNB mRNA (Figure S6D). However, JAM3 depletion decreased the total levels of LMNA protein (Figure S6E), but not LMNB protein (Figure S6F). The amount of LMNA protein in the nuclear lamina (Figure 8D, F) and total LMNA protein levels (Figure S6E) were rescued by the triple knockdown. These data support a model where the nuclear shape changes observed in JAM3 depleted cells are partially due to do decreases in LMNA protein, and a change in the LMNA:LMNB ratio.

Because phosphorylation of LMNA promotes the dissociation of LMNA filaments[78, 79], we measured the phosphorylation of Serine 22 on endogenous LMNA protein (hereafter referred to as pLMNA) following JAM3, SYNE4 and/or KIF5B. Depletion of JAM3 significantly increased the total levels of pLMNA (Figure 8G). Increased pLMNA levels were completely rescued in the triple knockdown. In summary, these data suggest that the phosphorylation of LMNA, and thus the amount of LMNA incorporated into the nucleus, is in part regulated by JAM3 and KIF5B-SYNE4 complexes that couple MTs to the nucleus.

JAM3 suppresses YAP/TAZ activation and EMT via nuclear mechanics

Interestingly, knocking down both YAP and TAZ rescued the decrease of LMNA protein in the nuclear matrix caused by JAM3 depletion (Figure 8D), but did not affect LMNB protein (Figure 8E). Moreover the total amounts of both LMNA (Figure S6E) and LMNB (Figure S6F) protein were markedly increased in JAM3/YAP/TAZ knockdown nuclei compared to both JAM3-depleted and control cells. Taken together these data suggest that YAP/TAZ activity in JAM3 depleted cells partly contributes to changes in LMNA protein levels.

To determine if changes in nuclear viscoelasticity underpinned the ability of JAM3-depleted cells to invade collagen gels, we monitored invasion in JAM3 cells co-depleted of LMNA or LMNB. Loss of LMNA alone promoted invasion and synergistically enhanced JAM3 knockdown cell invasion (Figure S6G). However, depletion of LMNB did not promote invasion or alter the ability of JAM3-depleted cells to invade (Figure S6I). Thus we conclude that decreases in LMNA protein levels, increases in pLMNA phosphorylation, and dissociation of LMNA filaments facilitate invasion following loss of JAM3.

To gain further insight into the role of Kinesin-1 function in regulating nuclear shape and LMNA levels and eliminate any possibly that KIF1B siRNA had off-target effects. We treated JAM3, or JAM3/SYNE4 deficient cells, with Rose Bengal Lactone (RBL) a fluorescein compound that binds Kinesin-1 at the L8/β5 pocket and inhibits the binding of Kinesin-1 to MTs[80]. RBL rescued nuclear morphology defects in both JAM3 and JAM3/SYNE4 depleted cells (Figure S7A,C), and the levels of LMNA in the outer matrix (Figure S7B,C). Thus we propose in epithelial cells the binding of Kinesin-1 to the MTs promotes nuclear morpheostasis, but in JAM3 depleted mesenchymal-like cells Kinesin-1 binding to the MTs promotes nuclear deformation. The effects of Kinesin-1 are mediated through its ability to regulate LMNA levels in the nuclear lamina.

JAM3 does not regulate the cell cycle or protect against DNA damage

To determine whether the JAM3-KIF5B-SYNE4-YAP/TAZ axis affects cell cycle progression, we quantified the percentage of G1, S, and G2 cells in cells depleted of: JAM3 alone; JAM3 in combination with KIF5B and/or SYNE4; or JAM3 in combination with YAP and TAZ (Figure S8A). We confirmed these observations by quantifying the number of mitotic cells (Methods; Figure S8B). JAM3 depletion had a very mild effect on cell cycle progression, with fewer cells in S/G2 but comparable numbers of mitotic cells to control populations. Knocking down either YAP or TAZ alone produced a small increase in G1 cells (Figure S8A), but combined depletion significantly reduced the number of mitotic cells (Figure S8B). Co-depletion of JAM3 did not rescue these phenotypes (Figure S8A and S8B). Spindle assembly appeared unaffected in JAM3 depleted cells (Figure S8C). Interestingly, both KIF5B and SYNE4 depletion alone had much more profound effects on cell cycle progression than JAM3 depletion, and these phenotypes were partial rescued by co-depletion with JAM3. (Figure S8A,B). We propose that uncoupling epithelial MTs from the nucleus (i.e. by KIF5B or SYNE4 RNAi), but not cell-cell adhesion complexes (i.e. by JAM3 RNAi), disrupts nuclear morpheostasis and cell cycle progression.

To determine if nuclear morphogenesis in JAM3 depleted cells defects increased DNA damage, we quantified the levels of gammaH2AX in wild-type cells or JAM3 knockdown cells co-depleted of KIF5B, SYNE4, KIF5B + SYNE4, YAP, YAP + TAZ, or TP53 (as a positive control of increased DNA damage). Only knockdown of TP53, SYNE4 or TAZ resulted in increased numbers of gammaH2AX levels (Figure S8D, S8E). Interestingly, while knockdown of JAM3 rescued the increased DNA damage observed in SYNE4 and TP53 depleted cells, it did not affect gammaH2Ax levels in the absence of TAZ. Taken together, these data suggest that nuclear morphogenesis defects in JAM3 depleted cells do not increase DNA damage.

JAM3 expression is associated with good prognosis

To validate JAM3's role as a tumour suppressor in patients, we performed survival analysis using JAM3 expression and disease-specific survival in different subgroups of breast cancer. We observed that in all subgroups with elevated levels of JAM3 (Luminal A, ILC, and Normal-like intrinsic subtypes), JAM3 expression is correlated with favourable prognosis (Figure 9A). Increased JAM3 expression also predicts relapse-free survival after treatment in patients with Luminal A type tumours (Figure 9B). Thus JAM3 is a *bona fide* tumour suppressor in breast cancer patients.

Given the ability of JAM3 depleted MCF10A cells to invade 3D matrices, we next sought to determine if JAM3 altered the metastatic potential of breast tumour cells in patients. Although

all forms of metastasis may not involve entry in a mesenchymal state[81-83], the metastasis of cells to stiff tissues such as bone likely requires matrix remodelling proteins such as MMPs whose levels are elevated following JAM3 depletion (Figure 3G)[84, 85]. Indeed, we observed a 1.6-fold increase of bone metastasis in cases with JAM3 loss compared with copy number neutral cases (Figure 9C), which suggests that cells with decreased levels of JAM3 have great invasive potential *in vivo*.

We reasoned that if KIF5B-SYNE4 mediated linkage of MTs to the nucleus is essential for nuclear shape changes following loss of JAM3, KIF5B and/or SYNE4 may be oncogenes. Indeed tumours with low JAM3 expression have high levels of KIF5B and SYNE4, whereas cells with high levels of JAM3 have low KIF5B and SYNE4 expression (Figure 9D). Moreover, increased KIF5B and SYNE4 copy numbers were observed in tumours with low JAM3 expression (Figure 9E). Finally, increased KIF5B and SYNE4 expression predicted shorter disease-specific survival periods (Figure 9F). Thus KIF5B and SYNE4 are oncogenes that antagonize the actions of the JAM3 tumour suppressor in patients.

Discussion

During the development and homeostasis of tissues such as the mammalian epidermis, epithelial cells establish apicobasal polarity, form extensive cell-cell contacts, downregulate the formation of focal adhesions (FAs); all which lead to a hexagonal, cube-like cell shapes. Dysregulation of epithelial tissue morphogenesis, such as caused by defects in cell-cell adhesion formation[86-88] and/or loss of apicobasal polarity[89-93] can trigger transcriptional programmes that lead to proliferation, invasiveness, and stem-like states[94, 95]. We show that disruption of normal cell-cell adhesion results in alteration in MT organization that can in turn deform nuclei, and upregulate the activity of transcriptional co-activators such as YAP/TAZ. These data provide a mechanistic basis for classic observations, such as those made by Elizabeth Hay[96], that disrupting cell-cell adhesion can cause cell fate changes.

More generally, our results point to an important role for cell-cell adhesions and MT organization in dictating the ability of the nucleus to resist deformation. The most parsimonious explanation for how alteration of cell-cell adhesion results in MT reorganization, is that components of cell-cell adhesion complexes, such as JAM3, are essential to capture and stabilize MTs, or even nucleate the polymerization of new MTs. Thus depletion of JAM3 results in detachment of MTs from the cell-cell adhesion complexes, and a “collapse” of MTs into a radial structure. Indeed JAM-A, which is highly related to JAM3 has been shown to bind the polarity proteins PAR3[97, 98], and PAR3 is critical for recruitment of MT nucleators such as gamma-tubulin to the apical membrane [99]. How the MTs can make such large deformations in

nuclear structure remain to be understood. Because MT plus-ends can still be coupled to the nucleus via KIF5B-SYNE4 complexes, MT polymerization/growth at plus-ends may generate forces that deform the nucleus. Alternatively, the forces may be a consequence of MT-bound motors such a kinesin or dynein[43]. In support of this idea, inhibiting the binding of Kinesin-1 to MTs by RBL rescues nuclear morphology in JAM3 deficient cells, and Kinesin-1 activity is required for nuclear deformation during constricted migration of *C. elegans* P-cells[46], and nuclear rotation during neuronal migration[76]. Thus the motor function of Kinesin-1 may be responsible for force generation on the nucleus.

Our observations, taken together with extensive previous work on Kinesin-1, suggest that Kinesin-1 function in nuclear morphogenesis differs based on cell type and the organization of the MT array. In epithelial cells, Kinesin-1 serves to physically couple SUN-KASH complexes to MT plus-end[75] (Figure 10). This coupling alone, and/or because of Kinesin-1 ATPase activity, positions nuclei and acts largely to prevent nuclear deformation. In contrast, in mesenchymal cells Kinesin-1 activity contributes to nuclear deformation (Figure 10). In mesenchymal cells Kinesin-1 is also likely being delivered to MT plus ends positioned at the leading edge of cells due the radial organization of MTs, delivers cargos that facilitate cell invasion[100, 101].

Importantly, our results open up a new avenue for breast cancer treatment. Uncoupling MTs from the nucleus in mesenchymal cells, prevents invasion, and remodelling of the ECM – but has little effect on cell survival. Thus uncoupling MT-nuclear connections and/or inhibiting Kinesin-1 activity may be suitable as part of differentiation-therapies – which aim not to kill mesenchymal/stem-like/drug-resistance cancer cells directly, but to revert them to an epithelial state which is less aggressive and/or more treatable with conventional therapeutics. In fact, given the prevalence of nuclear pleomorphism in other cancers, and other diseases, targeting MTs and MT-nuclear complexes may be a broadly applicable therapeutic strategy.

Author Contributions

M.G.-A, Y.Y., and C.B. designed the research. M.G.-A performed MCF10A experiments and analysed all experimental data. Y.Y. performed the bioinformatics analysis. R.R. Performed the sub fractionation experiments. J.E.S. wrote the script to segment donut nuclei. M.G.-A, Y.Y., and C.B. wrote the manuscript.

Acknowledgements

We thank F. Wallberg for assistance with image analysis and R. Patel for cytometry help (Flow Cytometry and Light Microscopy Facility, ICR, London, UK). We also thank A. Sadok (Cancer Therapeutics, ICR, London, UK) for technical help in bottom to top invasion assays. We thank J. Mansfield (TU-Dresden) for the MCF10A-PCNA cell line. We are grateful to Lucas Dent (ICR) for comments on the manuscript. This project was initiated by Y.Y. in the laboratory of Florian Markowetz (Cancer Research UK Cambridge Institute). Y.Y. is supported by a Cancer Research UK Career Establishment Award (C45982/A21808), Breast Cancer Now (2015NovPR638), NIH U54 CA217376, R01 CA185138, CDMRP Breast Cancer Research Program Award BC132057, Wellcome Trust (105104/Z/14/Z), and The Royal Marsden/ICR National Institute of Health Research Biomedical Research Centre. C.B. is supported by a Stand Up to Cancer UK Programme Foundation Award (C37275/1, A20146) and a CRUK/EPSRC Multidisciplinary Research Award (NS/A000062/1).

Methods

CONTACTS FOR REAGENT AND RESOURCE SHARING

Further information and requests for resources and reagents should be directed to and will be fulfilled by the Lead Contacts, Chris Bakal (Chris.Bakal@icr.ac.uk), Yinyin Yuan (Yinyin.Yuan@icr.ac.uk) and Mar Arias-Garcia (Mar.AriasGarcia@icr.ac.uk).

EXPERIMENTAL MODEL AND SUBJECT DETAILS

EXPERIMENTAL MODEL AND SUBJECT DETAILS

Cell lines and Cell Culture

MCF10-A cells were obtained from ATCC and MCF10-A mRuby-PCNA cells were a gift from J. Mansfeld (Technische Universität Dresden). They were cultured in DMEM/F12 supplemented with 5% Horse Serum, 10 µg/ml insulin, 20 ng/ml epidermal growth factor, 100 ng/ml cholera toxin, 500 ng/ml hydrocortisone and 100 mg/ml penicillin/ streptomycin. Cells were used between passages 4 and 15. hTERT-RPE1 cells were obtained from ATCC and cultured in DMEM, 10% heat-inactivated FBS and 100 mg/ml penicillin/ streptomycin.
All cell lines were confirmed to be mycoplasma-negative (e-Myco Mycoplasma PCR Detection Kit, iNtRON Biotechnology). Passage was carried out using 0.25% trypsin-EDTA (GIBCO) followed by centrifugation (1000 rpm, 4 min) and resuspension in complete medium. Cell counting was performed using Countess automated cell counter with trypan blue exclusion (Thermo).

Clinical samples

Primary frozen breast tumors were collected and stained independently in different laboratories contributing to the METABRIC consortium. All patient specimens were obtained with appropriate consent from the relevant institutional review board. All METABRIC samples used in this study (n=1026) included H&E images and molecular data passing quality control. Control DNA from match normal breast tissues was available for 473 samples and RNA from

144 of these individuals. All histopathological images were scanned with a ScanScope TX scanner (Aperio Technologies Inc.) providing images at 200-fold magnification. DNA and RNA were extracted from each primary tumor specimen and subjected to copy number and genotype analysis on the Affymetrix SNP 6.0 platform and transcriptional profiling on the IlluminaHT-12 v3 platform (Illumina_Human_WG-v3).

Pathological image analysis

To facilitate objective extraction of nuclear morphological features for tens of thousands of cells in a histological section, we performed automated image analysis on 1,026 H&E images of breast primary tumour whole sections using a previously described pipeline [102]. In brief, this pipeline segmented and classified nuclei into cancer, lymphocyte, and stromal cells based on their morphological features. To remove batch effects as a result of H&E slides batch processing, we normalized scores after subtracting median value of the batches by which images H&E were stained and scanned.

Following cell nuclei segmentation and classification, six nuclear shape features were used for each cancer cell nucleus, which include acircularity (*acirc*) and Hu's first moment or I1 (*I1*) both measuring shape irregularity. While acircularity is mathematically defined as the fraction of object area outside of a circle of the same size of area as the object, *I1* is equivalent to the moment of inertia and considers not only the shape but also the distribution of mass in the object. Hu's first moment or I1, known as the moment of inertia in mechanics, has been used to define an object's resistance to rotation in physics. In 2D images, pixel density is equivalent to physical mass within an object.

.

$$I1 = \mu_{02} + \mu_{20},$$
$$\mu_{pq} = \iint x^p y^q f(x,y) dxdy$$

where *f(x,y)* is the image segment. This morphological feature, when applied to nucleus image, represents nuclear irregularity not only in shape but also in the nuclear mass distribution.

Construction of a hybrid network

Significant associations followed by FDR correction between 18 morphological scores and RNA expression of 1000 cis-driven genes were used to construct a large network. Small network module shown in Figure 1B was constructed by removing associations with q-value greater than 0.005. Degree of connectivity was assessed for each morphological score, based on their connections with genes within the large network as well as the small network module.

RNAi transfections and drug treatments

RNAi experiments were performed by using the siRNA oligonucleotides from Dharmacon (see Supplemental Table S5 for the sequences). Cells were reverse-transfected in either 384-well, 96-well, or 6 wells plates or T25 flask either with single siRNAs or combinations thereof. 2 days later cells were either fixed or harvested for the bottom to top invasion assays, organotypic experiments, mRNA extraction, protein extraction or cytometry.

The majority of experiments were performed in 384-well Cell Carrier plates using MCF10A cells by using an in lab optimized screen protocol. Two siRNAs targeting *ECT2* and *PLK1* at several concentrations were used as transfection controls in order to test the efficiency of the transfection. Cell density and transfection times were assessed. The output of multinucleated cells for cells lacking *ECT2*, cell death for cells lacking *PLK1* and cell number was used to choose the best conditions. In order to transfect cells in the other 3 formats, all the reagents and cells were scaled up from the 384-well format according to the surface area and concentration in order to keep the same conditions across all the culture conditions.

All the siRNAs were used at a final concentration of 20nM. Briefly, 5uL per well of OptiMEM (GIBCO) containing 40 nL/well Lipofectamine RNAiMAX (Invitrogen) were mixed with 5uL per

well of OptiMEM containing also 40 nL/well of one single siRNA or combinations. The mix was incubated for 30-40 min at room temperature to allow the siRNA- Lipofectamine RNAiMAX complexes to form. Then, 30 uL of 4/3X Transfection media (to give 1X final concentration of serum and growth factors) containing cells were plated on top of the complexes at $3x10^4$ cells/ml. For the experiments regarding YAP/TAZ immunofluorescence a density gradient of mock-transfected cells (375, 750 and 1500 cells per well) was plated to use as a density regression curve (S8P and S8Q). siRNAs targeting *YAP1*, *TAZ*, *LMNA*, *LMNB* were also used to confirm gene knockdown and antibody specificity (supplemental 2 and 3). All the 2D experiments were performed by using at least 4 wells per condition per experiment, and at least two independent biological replicates were performed for all the imaging experiments.
Rose Bengal Lactone was used at 20uM and 40uM for 48 hours. Transforming Growth Factor-β1 was used 5ng/mL for 48 hours. The broad-spectrum MMP inhibitor GM6001 was used at 10uM for 24 hours before fixing the bottom to top invasion assays in collagen.

Fixation and immunofluorescence in 2D.
Following two days of incubation, cells were fixed either in pre-warmed 4% formaldehyde (ThermoScientific) in PBS for 15 min at room temperature (RT) or with cold MeOH for 10 min (anti-JAM3 or anti EB1). After fixation, cells were washed three times in PBS and then permeabilised in 0.2% Triton X-100/PBS solution for 15 min at RT (this step was not done for MeOH fixed samples or PFA-fixed samples that were going to be inmunostained with fibronectin). Following three washes in PBS, cells were blocked for 1 h in 2% bovine serum albumin (BSA) (Sigma)/PBS solution at RT. When using both mouse and rat primary antibodies in the same sample, sequential immunostaining was performed to avoid any antibody cross-reactions. Typically co-immunostaining with a mouse, rat and rabbit antibody was used. After the Block step, BSA was removed and the desired mouse primary antibody was added in Antibody solution (0.5%BSA/0.01% Triton X-100/PBS) at the indicated dilutions: Anti-β-Catenin Clone 14/Beta-Catenin (BD Biosciences, 1:1000), anti-Lamin A (Abcam, 1:1000), JAM-C (Santa Cruz, 1:200), EB1 Antibody (Santa Cruz, 1:100), YAP (G6) (Santa Cruz, 1:200), YAP/TAZ [67.3] (Santa Cruz, 1:1000). All the primary antibodies immunostaining was performed overnight at 4 °C. Then cells were washed three times in PBS and incubated with a goat anti-mouse antibody 1:1000 in Antibody solution for 2h at RT. Cells were washed three times in PBS and incubated with a rat anti-tubulin alpha antibody (Bio Rad, 1:1000) and an anti-rabbit primary antibody when applied, for 2 hours at RT. The anti-rabbit primary antibodies were used at the indicated dilutions: Phospho-Lamin A/C (Ser22) (Cell Signalling, 1:800), TAZ (V386) (Cell Signalling, 1:200), Collagen I alpha 1 (Novus Biologicals, 1:500), Phospho-Histone H2A.X (Ser139) Antibody (Cell Signalling, 1:1000), Anti-Lamin B1 (Abcam, 1:1000). Then cells were washed three times in PBS, and incubated for 2h at room temperature with a goat anti-rat antibody and/or a goat anti-rabbit antibody or Alexa-647 phalloidin (Invitrogen) if needed. For the anti-goat Lamin B Antibody (Santa Cruz, 1:500) a single immunostaining was performed with a donkey anti-goat secondary antibody and Alexa-568 phalloidin. For the anti-human Fibronectin immunostaining (Dako, 1:1000) a single immunostaining was performed with a goat anti-rabbit secondary antibody and Alexa-568 phalloidin. Finally, to stain nuclei, a 1:1000 dilution of DAPI (4',6-diamidino-2-phenylindole, dihydrochloride, Molecular Probes; D1306, Molecular Probes)/PBS solution or 5 mg/ml Hoescht (Invitrogen)/PBS solution was carried out for 15 min at RT. 384-well plates were sealed for imaging with an Opera Cell:Explorer-automated spinning disk confocal microscope (PerkinElmer) in the magnification indicated in the figure legends. At least twenty fields at random positions per well of a 384-well plate were imaged.

Bottom-Top Invasion screens in a Collagen matrix
MCF10A cells were transfected with 20nM of RNAi for 48h as described above. Then cells were trypsinized and suspended in a solution of NaOH, DMEM 5x and bovine collagen I (Purecol) at 2.3 mg/ml to a final concentration of 5 × 104 cells/500 µl. Bovine collagen

neutralization at pH=7 was confirmed in all the experiments performed. One hundred microliter aliquots per well of neutralized collagen solution were dispensed into chilled Cell carrier 96-well plates followed by a centrifugation at 1000 rpm at 4°C for 5 minutes to ensure all cells were at the bottom of the plate. Then, plates were incubated at 37°C and 80% humidity for 3h to allow the collagen to polymerize. Importantly, the outer wells were also filled with sterile water or PBS to prevent gel dehydration and edge effects due to evaporation. Then 50uL of growth media 3X containing 30uM of the pan MMP inhibitor GM6001 or DMSO was added on the top to stimulate cell invasion. After 24 h of incubation at 37°C, cells were fixed at room temperature with 50 uL per well of 16% Methanol-free paraformaldehyde plus 5 µg/ml Hoechst 33258 for 24 h. Samples were run in quadruplicate for each condition and repeated twice in experiments separated by several months. Inmunostaining was performed with 1:500 phalloidin/ PBS solution overnight with a previous permeabilization step with NP40 at 0.5% at 4°C for 30 minutes. Plates were sealed and imaged with an Opera Cell:Explorer-automated spinning disk confocal microscope (PerkinElmer) and using a 20× air objective lens (NA = 0.45). Three Confocal Z slices were collected from each well at 0 µm (bottom of well), 30 µm (middle of the well) and 60 µm (top of the well) and at least 20 fields were imaged in every Z stack position in each well avoiding the edge fields.

Invasion of Organotypic cultures in a Matrigel:Collagen matrix

The morphogenesis assay was adapted from [103]. Briefly, previously chilled eight-well culture slides (Falcon) or cell carrier 96 wells plates were coated with a thick layer (150-200uL/cm2) of a mix of growth factor-reduced (GFR) Matrigel (BD Biosciences) and neutralized Bovine Collagen I (Purecol) yielding a final collagen concentration of 1 mg/mL and a final Matrigel gel mix concentration of 5 mg/mL. The stock solutions of all the Matrigel vials used to perform the experiments of this manuscript were 10 mg/mL at least (See Supplemental Table S3 for the lot numbers used). Importantly, all the surrounding wells were also filled with water or PBS and the ECM was gelled for 3 hours in a standard 37 °C humidified cell culture incubator with a 5% CO_2 environment. Then, a single MCF10A cell suspension (4000 cells/well for 96 wells plate or 8000 cells/well for 8 wells chambers at 2*104 cells/mL) was plated on top of the pre-polymerized Matrigel:collagen matrix in acini assay medium. This assay media is composed of phenol red free DMEM supplemented with cholera toxin, hydrocortisone, insulin and penicillin/ streptomycin at the same concentrations than the growth media and 2%horse serum, 5 ng/ml of EGF and 2mg/mL of Matrigel. Unless otherwise stated, the acini morphology data refers to the structures observed 2 days after the 3D experiment started and 4 days after the cells were transfected with siRNA. When acini were cultured for 4 days or 8 days, assay medium was replaced every 2-3 days. Thus 4 or 8 days of acini growth in the main text corresponds to 6 or 10 days after the siRNA transfection. Acini were fixed in 4% Methanol-free paraformaldehyde and 5 µg/ml Hoechst 33258 for 15 min at RT. Inmunostaining was performed with Laminin-5 Antibody (P3H9-2) (Santa Cruz, 1:1000) and anti-Fibronectin (Dako, 1:1000) in Block solution (4% BSA) plus 0,05% of Tween20 overnight at 4 degrees with a previous permeabilization step with 0.5% Triton X-100/PBS solution for 30 min at RT and blocked in 4% BSA for 2 hours at RT. Acini were washed 3 × 20 minutes in PBS and then incubated with a goat anti-mouse 568 antibody and with a goat anti-rabbit 488 antibody in block solution plus 0,05% tween20 for 1 h at room temperature. Acini were washed 3 × 20 minutes in and finally a 1:500 phalloidin 647/ PBS solution was added either to the 8-well chamber or to the 96-well plate, sealed and left overnight at 4 degrees. 8 -well chamber slides were rinsed in PBS, mounted in Vectashield (H-1000, Vector Laboratories) and the coverslip was sealed with clear nail varnish. Slides were imaged using either a Zeiss 710 LSM Confocal microscope or a Leica SP2 confocal scanning microscope (Leica Microsystems, Milton Keynes, Bucks, UK) at 20x or ×40 oil immersion lens as indicated in the figure legends. At least 400 acini were counted by eye and classified according to their shape in normal acini (round) or abnormal shape (general loss of spherical geometry and/or protrusions). See the figure legends for more details. 96 well plates were sealed and imaged with an Opera Cell:Explorer-automated spinning disk confocal microscope (PerkinElmer) and using a 20× air objective lens (NA = 0.45). Several Confocal Z

slices were collected from the bottom to the top of the acini and they were summed to create a projection of the image (maximum projection). At least 9 fields were imaged per well. Importantly only the middle and symmetrical fields were imaged avoiding possible lateral interactions of the acini with the plastic sides of the culture dish.
Live imaging experiments in 3D were performed in a humidified CO2 chamber with a Nikon Time-Lapse 2000 wide field Microscopy with a 10× Magnification. Single cells were mock transfected or treated with JAM3 siRNA for 24 hours. The following day, cells were trypsinized and plated on top of a Matrigel:collagen mix as described above and let them to settle overnight in a cell culture incubator before starting the live imaging experiment. Acini were imaged by using the brightfield and frames were taken each 10 minutes for 2 days. At least 8 fields were imaged per condition. Thus, the acini were at day 1 when live filming began and 2 days post siRNA transfection.

Cell Segmentation, shape feature extraction and analysis of 2D and 3D experiments
Image acquisition and cell segmentation was performed using Columbus high-content image analysis software or Acapella (donut nuclei segmentation). 'Whole Nuclei' were segmented using the Hoechst or DAPI channel (Figure S9A). Since several siRNAs produced holes in the nuclei of the cells, the nucleus region used for all the experiments of this manuscript was limited to 2 to 2.5 um from the border of the whole nuclei, avoiding to consider the holes as part of the nuclei and named as 'nuclei' or 'Inner nuclei' (Figure S9B, S9L). The perinuclear region, defined as a region encompassing 1.5 to 2.5 um from the border of the whole nuclei, was used to measure cytoplasmic intensity (Figure S9C).
For all the 2D experiments, cell bodies were segmented using the tubulin channel (Figure S9D) except for the soluble fibronectin determination where the actin channel was used. Neighbour fraction (NF) was determined as the proportion of a cell's border in contact with other cells and defined by the mathematical formula: 1- (B/2*A) where A and B are the areas of two membrane regions: 'region A' 0 to 1 px2 (Figure S9E) and 'region B' -1 to 0 px2 (Figure S9F). Mitotic cells were filtered using a combination of Hoechst intensity mean and Hoechst intensity maximum and excluded of all the analysis (Figure S9G). The border objects were also removed from the analysed cells considering only cells completely imaged (Figure S9H). The **percentage of donut nuclei** was performed using Acapella or Columbus (PerkinElmer). Whole Nuclei were segmented based on the Hoechst channel. The mean intensity and the size of the nuclei was calculated and the holes were detected by a threshold mask for Hoechst intensity (Figure S9I). Results are presented as percentage of the population with a donut nuclei. To select the cells with low Nuclear Roundness, a threshold of Nuclear Roundness < 0.85 was established within the non donut population, hence excluding the cells having a donut nuclei.
For the **Lamin A and Lamin B** measurements, both, the Inner and Outer area of the nuclei were considered. Whole Nuclei were segmented based on the Hoechst channel (S8J). The outer region of the nuclei or nuclear envelope area, was defined as a region encompassing 0 to 0,5 um from the border of the nuclei, and matched with the maximum antibody intensity in the nuclear membrane (Figure S9K). For the **Phospho-Lamin A to Lamin A** ratio determination, the intensity of the P-Lamin in the Inner region or nucleoplasm (Figure S9L) was divided by the intensity of Lamin A in the outer region of the nuclei or nuclear membrane (Figure S9K). To measure the **soluble fibronectin,** the Find image region module was used to segment the cells based on the actin channel (Figure S9M) and considering as a unique region defined as 'colony area' or area within cells. This was used as the reference area to segment the 'area outside of the colony' where the intensity of the Fibronectin channel was measured and normalized to the area without cells (Figure S9N). The **collagen spots** number was determined using the Spot finder module. The spots were found based on the collagen channel and those with a radius size same or greater than 2 um and a contrast intensity greater than 0,7 were considered as collagen spots (Figure S9O) and normalized to the cell area. **YAP and TAZ** ratios were calculated as the $\log_{10}$ of the mean Inner nuclear intensity/mean perinuclear region intensity per cell. YAP and TAZ ratios were corrected for cell number on mock-transfected cells by using a linear regression analysis (Sero et al., 2015). In each

experiment, different numbers of mock transfected cells were plated to cover the range of densities of siRNA transfected cells (Figure S9P). The observed value for the $\log_{10}$ TAZ nuc/cytop ratio or $\log_{10}$ YAP nuc/cytop ratio was measured and corrected by using the linear regression equation and the observed minus predicted value was plotted in all the figures of this manuscript (Figure S9Q). For the **EB1 distribution**, the Radial Mean intensity of the signal was considered. This is defined as the mean object radius based on the EB1 intensity values weighted by the distance from the mass center of the cell. For the bottom to top invasion assays, nuclei were segmented as above and cell cores were segmented on the actin channel. A contrast threshold for the Inner nuclei was chosen for every experiment (commonly 0,50) to select only cells that were really in the selected plane to avoid quantifying the same cell in several planes (Figure S10I). A Second step to filter cells was performed by excluding the cells were the mean of the actin Intensity in the perinuclear area was lower than 150. Figure S10BII). The invasion index was calculated as the sum of the number of cells at 30 µm plus 60 µm and divided by the total number of cells (0 µm + 30 µm + 60 µm).
For the organoids segmentation, the Find image region module was used to define the area of the core of the organoids based on the actin channel and split into objects as a population named 'colonies' (Figure S10AI). Then, within that population, cells were found based on the Hoechst channel (Figure S10AII). This feature was used to classify the colonies population according to the **number of cells per colony**, in Single cells (One nuclei per colony) or Acini, as two or more nuclei per colony (Figure S10AIII). Further characterization of organoids was carried out exclusively in the Acini population: f**ibronectin** mean intensity of the Acini body area was measured and normalized to the mean area of the Acini. **Actin protrusions or spikes** were determined by using the Find neurites modulus and based on the actin channel (Figure S10AVI). To perform all the analysis in 3D, the maximum projection was used.

Cell cycle analysis by Flow Cytometry.
MCF10A cells were transfected with the appropriate siRNAs 48h prior to the start of the cell cycle analysis. Cell cycle profiling using propidium iodide (PI) staining was performed according to standard procedures. Briefly, cells were harvested and washed once in cold PBS. Prior to the staining, cells were fixed with cold 80% ethanol and stabilized overnight at −20°C. After 2 washes in cold PBS, cells were finally resuspended in a PI staining mix (40 µg/mL propidium iodide, 0.1% triton X-100, 5 U/mL RNAse A and PBS 1X) and incubated at 37 °C for 30 min. FACS analysis was performed on an LSRII station (Becton Dickinson). At least 10.000 cells per condition were gated by duplicate for each condition. Data were obtained using the FlowJo cytometry package using raw cytometry data and 3D histograms were generated.

Subcellular fractionation and immunoblotting.
The Subcellular Protein Fractionation Kit for cultured cells (ThermoFisher) was used to isolate the cytoplasm, membrane, soluble nuclear fraction, chromatin-bound and cytoskeletal protein extracts. MCF10A cells were harvested and washed by suspending the cell pellet with ice-cold PBS. Then, 1% NP-40/0.1% SDS lysis buffer (50 mM Tris 7.4, 150 mM NaCl, 1mM EDTA) with protease and phosphatase inhibitor cocktail (Thermo) was added. Protein concentrations of the subcellular protein fraction lysates were measured using Pierce BCA Protein Assay Kit (ThermoFisher). Samples were boiled for 10 minutes and the extracts were separated by SDS-polyacrylamide gel electrophoresis using precast 4–20% Precise protein gels (ThermoScientific). Separated proteins were transferred to PVDF-FL transfer membrane (Merck Millipore) at 40V for 90 min at 4 °C. PVDF membranes were blocked in 5% milk/TBS 10% glycerol + 0.05% tween20 (Sigma-Aldrich) (TBS/t) or 5% BSA/TBS 10% glycerol + 0.05% TBS/t for 1 hr at RT on a rolling shaker, then incubated in the appropriate primary antibodies: Mouse anti-GAPDH (Novus Biologics, 1:2000), Mouse anti-LMNA (Abcam, 1:500), Mouse anti-PCNA (Santa Cruz, 1:1000), Rabbit anti-KIF5B (Proteintech, 1:1000), Mouse anti-Beta Tubulin (Sigma, 1:1000) and Mouse anti-YAP/TAZ (Santa Cruz, 1:1000) overnight at 4 °C on a rolling shaker, washed 3 × 20 min in TBS/t before incubating for 1 hr at RT in secondary anti-rabbit HRP-linked antibody and/or anti-mouse HRP-linked antibody (Cell Signalling) on a

rolling shaker. Membranes were washed 3 × 20 min in TBS/t, 1x in PBS for 5 min and then soaked in an enhanced luminol-based chemiluminescent substrate for detection of horseradish peroxidase (HRP) on immunoblots before visualising on the Azure c300 scanner. Western Blot analysis were performed using Image J and Excel. JAM3 protein depletion after RNAi treatments was confirmed also by Western Blotting carried out as above. Whole cell lysates were obtained by directly exposing cells to sodium dodecyl sulphate (SDS) lysis buffer supplemented with phosphatase and protease inhibitors (Roche). Membranes were incubated in Roti block (Roth) containing the primary antibodies JAM3 (Santa Cruz, 1:500) and B-actin (Sigma, 1:5000) overnight at 4 °C, washed 3 × 20 min in TBS/0.05% TritonX-100 (TBS/t) and then incubated for 1 hr in Roti block containing the above anti-mouse HRP-linked antibody. Images were generated by using an X-ray Film Processor.

RNA extraction, PCR Array Human Epithelial to Mesenchymal Transition (EMT) and qRT–PCR

Total RNA was extracted using the standard phenol-chloroform procedures (Trizol) and the RNeasy kit (Qiagen). For the RT² Profiler™ PCR Array Human Epithelial to Mesenchymal Transition kit (EMT) (Qiagen), RNA integrity of all the samples was tested by using the Agilent RNA 6000 Nano kit (Agilent Technologies, Cheshire, UK) and measured with an Agilent Bioanalyser. The RNA integrity number (RIN) was calculated by using the Agilent 2100 software. Briefly, 400 ng of each RNA was used following supplier's recommendations and carried out on a Quant 6 RT PCR (Applied Biosystems). Gene expression data was analyzed by excel and normalized to the mock transfected values. Gene expression numbers lower than 0,5 were considered as downregulated and genes with values greater than 1,3 were considered as upregulated. Heat maps were generated by using the Morpheus software (https://software.broadinstitute.org/morpheus). Panel of genes included in the EMT kit and results are showed in the Excel file 1, RT² Profiler™ PCR Array Human EMT_Cat# PAHS-090Z_Data related to Fig3G_Gene expression of JAM3 siRNAs. The conventional Quantitative real time polymerase chain reaction (qRT-PCR), was performed using cDNA made from extracted RNA. Briefly, 250 ng of purified RNA was converted to cDNA by using the High-Capacity RNA-to-cDNA Kit (Applied Biosystems) according to the manufacturer's protocol. qRT-PCR analysis was carried out using the SYBRGreen PCR Master Mix (Invitrogen) following supplier's recommendations, on a 7300 AB system (Applied Biosystems) or a Quant 6 RT PCR (AppliedBiosystems). ΔΔCt quantification was performed on at least triplicate absolute measurements and normalized to GAPDH mRNA. PCR primers are listed in table S3.

Statistics and Reproducibility

All data generated in this manuscript was derived from at least two independent experiments and are presented as means ± SEM. Comparisons among groups were performed using GraphPad Prism version 6.00 and 7.00, GraphPad Software, La Jolla California USA, www.graphpad.com. Analysis of regression lines and R^2 values (Pearson's correlation) and qRT-PCR analysis were performed with Excel. Statistical details of experiments can be found in the legends.

Survival analysis was performed with breast cancer–specific 10-year survival data. Kaplan-Meier estimator was used for patient stratification where log-rank test was used for testing difference among groups. Cox proportional hazards regression model was fitted and 95% confidence intervals were computed to determine the prognostic values, where log-rank test with $P < 0.05$ was considered significant. Correlation was computed with Pearson correlation and q-values computed using False Discovery Rate (FDR) correction using R package fdrtool in the situation of multiple correlation analysis. Test for significant differences among groups of a single variable was carried out using ANOVA. Tests for trend of a continuous variable among groups were performed with Jonckheere's Trend test for a null hypothesis that a variable does not follow a monotone trend set by the groups

References

1. Dahl, K.N., Ribeiro, A.J. & Lammerding, J. Nuclear shape, mechanics, and mechanotransduction. *Circulation research* **102**, 1307-1318 (2008).
2. Fedorchak, G. & Lammerding, J. Cell Microharpooning to Study Nucleo-Cytoskeletal Coupling. *Methods in molecular biology* **1411**, 241-254 (2016).
3. Irianto, J. *et al.* Nuclear constriction segregates mobile nuclear proteins away from chromatin. *Mol Biol Cell* **27**, 4011-4020 (2016).
4. Irianto, J. *et al.* DNA Damage Follows Repair Factor Depletion and Portends Genome Variation in Cancer Cells after Pore Migration. *Curr Biol* **27**, 210-223 (2017).
5. Cho, S., Irianto, J. & Discher, D.E. Mechanosensing by the nucleus: From pathways to scaling relationships. *J Cell Biol* **216**, 305-315 (2017).
6. Wang, X. *et al.* Mechanical stability of the cell nucleus - roles played by the cytoskeleton in nuclear deformation and strain recovery. *J Cell Sci* **131** (2018).
7. Stephens, A.D. *et al.* Physicochemical mechanotransduction alters nuclear shape and mechanics via heterochromatin formation. *Mol Biol Cell* **30**, 2320-2330 (2019).
8. Kim, D.H., Cho, S. & Wirtz, D. Tight coupling between nucleus and cell migration through the perinuclear actin cap. *J Cell Sci* **127**, 2528-2541 (2014).
9. Khatau, S.B. *et al.* A perinuclear actin cap regulates nuclear shape. *Proc Natl Acad Sci U S A* **106**, 19017-19022 (2009).
10. Thiam, H.R. *et al.* Perinuclear Arp2/3-driven actin polymerization enables nuclear deformation to facilitate cell migration through complex environments. *Nature communications* **7**, 10997 (2016).
11. Haase, K. *et al.* Extracellular Forces Cause the Nucleus to Deform in a Highly Controlled Anisotropic Manner. *Scientific reports* **6**, 21300 (2016).
12. Tremblay, D., Andrzejewski, L., Leclerc, A. & Pelling, A.E. Actin and microtubules play distinct roles in governing the anisotropic deformation of cell nuclei in response to substrate strain. *Cytoskeleton* **70**, 837-848 (2013).
13. Cho, S. *et al.* Mechanosensing by the Lamina Protects against Nuclear Rupture, DNA Damage, and Cell-Cycle Arrest. *Dev Cell* **49**, 920-935 e925 (2019).
14. Bianchi, A., Manti, P.G., Lucini, F. & Lanzuolo, C. Mechanotransduction, nuclear architecture and epigenetics in Emery Dreifuss Muscular Dystrophy: tous pour un, un pour tous. *Nucleus* **9**, 276-290 (2018).
15. Butin-Israeli, V., Adam, S.A., Goldman, A.E. & Goldman, R.D. Nuclear lamin functions and disease. *Trends Genet* **28**, 464-471 (2012).
16. Robijns, J., Houthaeve, G., Braeckmans, K. & De Vos, W.H. Loss of Nuclear Envelope Integrity in Aging and Disease. *International review of cell and molecular biology* **336**, 205-222 (2018).
17. Worman, H.J. Nuclear lamins and laminopathies. *The Journal of pathology* **226**, 316-325 (2012).
18. Eriksson, M. *et al.* Recurrent de novo point mutations in lamin A cause Hutchinson-Gilford progeria syndrome. *Nature* **423**, 293-298 (2003).
19. Starr, D.A. & Fridolfsson, H.N. Interactions between nuclei and the cytoskeleton are mediated by SUN-KASH nuclear-envelope bridges. *Annu Rev Cell Dev Biol* **26**, 421-444 (2010).
20. Simon, D.N. & Wilson, K.L. The nucleoskeleton as a genome-associated dynamic 'network of networks'. *Nat Rev Mol Cell Biol* **12**, 695-708 (2011).
21. Swift, J. & Discher, D.E. The nuclear lamina is mechano-responsive to ECM elasticity in mature tissue. *J Cell Sci* **127**, 3005-3015 (2014).
22. Kirby, T.J. & Lammerding, J. Emerging views of the nucleus as a cellular mechanosensor. *Nat Cell Biol* **20**, 373-381 (2018).
23. Dauer, W.T. & Worman, H.J. The nuclear envelope as a signaling node in development and disease. *Dev Cell* **17**, 626-638 (2009).

24. Sero, J.E. *et al.* Cell shape and the microenvironment regulate nuclear translocation of NF-kappaB in breast epithelial and tumor cells. *Molecular systems biology* **11**, 790 (2015).
25. Elosegui-Artola, A. *et al.* Force Triggers YAP Nuclear Entry by Regulating Transport across Nuclear Pores. *Cell* **171**, 1397-1410 e1314 (2017).
26. Pfeifer, C.R., Alvey, C.M., Irianto, J. & Discher, D.E. Genome variation across cancers scales with tissue stiffness - an invasion-mutation mechanism and implications for immune cell infiltration. *Current opinion in systems biology* **2**, 103-114 (2017).
27. Bakhoum, S.F. *et al.* Chromosomal instability drives metastasis through a cytosolic DNA response. *Nature* **553**, 467-472 (2018).
28. Lim, S., Quinton, R.J. & Ganem, N.J. Nuclear envelope rupture drives genome instability in cancer. *Mol Biol Cell* **27**, 3210-3213 (2016).
29. Chow, K.H., Factor, R.E. & Ullman, K.S. The nuclear envelope environment and its cancer connections. *Nature reviews. Cancer* **12**, 196-209 (2012).
30. Bussolati, G. Proper detection of the nuclear shape: ways and significance. *Romanian journal of morphology and embryology = Revue roumaine de morphologie et embryologie* **49**, 435-439 (2008).
31. Pfeifer, C.R., Irianto, J. & Discher, D.E. Nuclear Mechanics and Cancer Cell Migration. *Advances in experimental medicine and biology* **1146**, 117-130 (2019).
32. Krause, M. & Wolf, K. Cancer cell migration in 3D tissue: negotiating space by proteolysis and nuclear deformability. *Cell adhesion & migration* **9**, 357-366 (2015).
33. Takaki, T. *et al.* Actomyosin drives cancer cell nuclear dysmorphia and threatens genome stability. *Nature communications* **8**, 16013 (2017).
34. Xia, Y. *et al.* Rescue of DNA damage after constricted migration reveals a mechano-regulated threshold for cell cycle. *J Cell Biol* **218**, 2545-2563 (2019).
35. Xia, Y. *et al.* Nuclear rupture at sites of high curvature compromises retention of DNA repair factors. *J Cell Biol* **217**, 3796-3808 (2018).
36. Patteson, A.E. *et al.* Loss of Vimentin Enhances Cell Motility through Small Confining Spaces. *Small*, e1903180 (2019).
37. Patteson, A.E. *et al.* Vimentin protects cells against nuclear rupture and DNA damage during migration. *J Cell Biol* (2019).
38. Bartolini, F. & Gundersen, G.G. Generation of noncentrosomal microtubule arrays. *J Cell Sci* **119**, 4155-4163 (2006).
39. Meads, T. & Schroer, T.A. Polarity and nucleation of microtubules in polarized epithelial cells. *Cell Motil Cytoskeleton* **32**, 273-288 (1995).
40. Akhmanova, A. & Hoogenraad, C.C. Microtubule minus-end-targeting proteins. *Curr Biol* **25**, R162-171 (2015).
41. Keating, T.J. & Borisy, G.G. Centrosomal and non-centrosomal microtubules. *Biol Cell* **91**, 321-329 (1999).
42. Shtutman, M. *et al.* Signaling function of alpha-catenin in microtubule regulation. *Cell Cycle* **7**, 2377-2383 (2008).
43. Wang, S., Reuveny, A. & Volk, T. Nesprin provides elastic properties to muscle nuclei by cooperating with spectraplakin and EB1. *J Cell Biol* **209**, 529-538 (2015).
44. Forth, S. & Kapoor, T.M. The mechanics of microtubule networks in cell division. *J Cell Biol* **216**, 1525-1531 (2017).
45. Wu, Y.K. & Kengaku, M. Dynamic Interaction Between Microtubules and the Nucleus Regulates Nuclear Movement During Neuronal Migration. *J Exp Neurosci* **12**, 1179069518789151 (2018).
46. Bone, C.R., Chang, Y.T., Cain, N.E., Murphy, S.P. & Starr, D.A. Nuclei migrate through constricted spaces using microtubule motors and actin networks in C. elegans hypodermal cells. *Development* **143**, 4193-4202 (2016).
47. Zhang, Q. *et al.* DOCK8 regulates lymphocyte shape integrity for skin antiviral immunity. *The Journal of experimental medicine* **211**, 2549-2566 (2014).
48. Isermann, P. & Lammerding, J. Consequences of a tight squeeze: Nuclear envelope rupture and repair. *Nucleus* **8**, 268-274 (2017).

49. Solovei, I. *et al.* Nuclear architecture of rod photoreceptor cells adapts to vision in mammalian evolution. *Cell* **137**, 356-368 (2009).
50. Seirin-Lee, S. *et al.* Role of dynamic nuclear deformation on genomic architecture reorganization. *PLoS computational biology* **15**, e1007289 (2019).
51. Lottersberger, F., Karssemeijer, R.A., Dimitrova, N. & de Lange, T. 53BP1 and the LINC Complex Promote Microtubule-Dependent DSB Mobility and DNA Repair. *Cell* **163**, 880-893 (2015).
52. Swift, J. *et al.* Nuclear lamin-A scales with tissue stiffness and enhances matrix-directed differentiation. *Science* **341**, 1240104 (2013).
53. Harada, T. *et al.* Nuclear lamin stiffness is a barrier to 3D migration, but softness can limit survival. *J Cell Biol* **204**, 669-682 (2014).
54. Ward, G.E. & Kirschner, M.W. Identification of cell cycle-regulated phosphorylation sites on nuclear lamin C. *Cell* **61**, 561-577 (1990).
55. Curtis, C. *et al.* The genomic and transcriptomic architecture of 2,000 breast tumours reveals novel subgroups. *Nature* **486**, 346-352 (2012).
56. Choy, B., LaLonde, A., Que, J., Wu, T. & Zhou, Z. MCM4 and MCM7, potential novel proliferation markers, significantly correlated with Ki-67, Bmi1, and cyclin E expression in esophageal adenocarcinoma, squamous cell carcinoma, and precancerous lesions. *Human pathology* **57**, 126-135 (2016).
57. Baxley, R.M. & Bielinsky, A.K. Mcm10: A Dynamic Scaffold at Eukaryotic Replication Forks. *Genes* **8** (2017).
58. Gartel, A.L. FOXM1 in Cancer: Interactions and Vulnerabilities. *Cancer research* **77**, 3135-3139 (2017).
59. Yasmeen, A., Berdel, W.E., Serve, H. & Muller-Tidow, C. E- and A-type cyclins as markers for cancer diagnosis and prognosis. *Expert review of molecular diagnostics* **3**, 617-633 (2003).
60. Marzec, K. & Burgess, A. The Oncogenic Functions of MASTL Kinase. *Frontiers in cell and developmental biology* **6**, 162 (2018).
61. Bakal, C., Aach, J., Church, G. & Perrimon, N. Quantitative morphological signatures define local signaling networks regulating cell morphology. *Science* **316**, 1753-1756 (2007).
62. Economopoulou, M. *et al.* Expression, localization, and function of junctional adhesion molecule-C (JAM-C) in human retinal pigment epithelium. *Invest Ophthalmol Vis Sci* **50**, 1454-1463 (2009).
63. Zen, K. *et al.* JAM-C is a component of desmosomes and a ligand for CD11b/CD18-mediated neutrophil transepithelial migration. *Mol Biol Cell* **15**, 3926-3937 (2004).
64. Lamagna, C. *et al.* Dual interaction of JAM-C with JAM-B and alpha(M)beta2 integrin: function in junctional complexes and leukocyte adhesion. *Mol Biol Cell* **16**, 4992-5003 (2005).
65. Aurrand-Lions, M., Johnson-Leger, C., Wong, C., Du Pasquier, L. & Imhof, B.A. Heterogeneity of endothelial junctions is reflected by differential expression and specific subcellular localization of the three JAM family members. *Blood* **98**, 3699-3707 (2001).
66. Nieto, M.A., Huang, R.Y., Jackson, R.A. & Thiery, J.P. Emt: 2016. *Cell* **166**, 21-45 (2016).
67. Piccolo, S., Dupont, S. & Cordenonsi, M. The biology of YAP/TAZ: hippo signaling and beyond. *Physiol Rev* **94**, 1287-1312 (2014).
68. Shiu, J.Y., Aires, L., Lin, Z. & Vogel, V. Nanopillar force measurements reveal actin-cap-mediated YAP mechanotransduction. *Nat Cell Biol* **20**, 262-271 (2018).
69. Shao, D.D. *et al.* KRAS and YAP1 converge to regulate EMT and tumor survival. *Cell* **158**, 171-184 (2014).
70. Lamar, J.M. *et al.* The Hippo pathway target, YAP, promotes metastasis through its TEAD-interaction domain. *Proc Natl Acad Sci U S A* **109**, E2441-2450 (2012).
71. Overholtzer, M. *et al.* Transforming properties of YAP, a candidate oncogene on the chromosome 11q22 amplicon. *Proc Natl Acad Sci U S A* **103**, 12405-12410 (2006).

72. Zhao, B. *et al.* TEAD mediates YAP-dependent gene induction and growth control. *Genes & development* **22**, 1962-1971 (2008).
73. Rajgor, D. & Shanahan, C.M. Nesprins: from the nuclear envelope and beyond. *Expert Rev Mol Med* **15**, e5 (2013).
74. Ketema, M. & Sonnenberg, A. Nesprin-3: a versatile connector between the nucleus and the cytoskeleton. *Biochem Soc Trans* **39**, 1719-1724 (2011).
75. Roux, K.J. *et al.* Nesprin 4 is an outer nuclear membrane protein that can induce kinesin-mediated cell polarization. *Proc Natl Acad Sci U S A* **106**, 2194-2199 (2009).
76. Wu, Y.K., Umeshima, H., Kurisu, J. & Kengaku, M. Nesprins and opposing microtubule motors generate a point force that drives directional nuclear motion in migrating neurons. *Development* **145** (2018).
77. Buxboim, A. *et al.* Coordinated increase of nuclear tension and lamin-A with matrix stiffness outcompetes lamin-B receptor that favors soft tissue phenotypes. *Mol Biol Cell* **28**, 3333-3348 (2017).
78. Heald, R. & McKeon, F. Mutations of phosphorylation sites in lamin A that prevent nuclear lamina disassembly in mitosis. *Cell* **61**, 579-589 (1990).
79. Buxboim, A. *et al.* Matrix elasticity regulates lamin-A,C phosphorylation and turnover with feedback to actomyosin. *Curr Biol* **24**, 1909-1917 (2014).
80. Hopkins, S.C., Vale, R.D. & Kuntz, I.D. Inhibitors of kinesin activity from structure-based computer screening. *Biochemistry* **39**, 2805-2814 (2000).
81. Fischer, K.R. *et al.* Epithelial-to-mesenchymal transition is not required for lung metastasis but contributes to chemoresistance. *Nature* **527**, 472-476 (2015).
82. Somarelli, J.A. *et al.* Distinct routes to metastasis: plasticity-dependent and plasticity-independent pathways. *Oncogene* **35**, 4302-4311 (2016).
83. Zheng, X. *et al.* Epithelial-to-mesenchymal transition is dispensable for metastasis but induces chemoresistance in pancreatic cancer. *Nature* **527**, 525-530 (2015).
84. Kang, Y. *et al.* A multigenic program mediating breast cancer metastasis to bone. *Cancer Cell* **3**, 537-549 (2003).
85. Esposito, M., Guise, T. & Kang, Y. The Biology of Bone Metastasis. *Cold Spring Harb Perspect Med* **8** (2018).
86. Vasioukhin, V., Bauer, C., Degenstein, L., Wise, B. & Fuchs, E. Hyperproliferation and defects in epithelial polarity upon conditional ablation of alpha-catenin in skin. *Cell* **104**, 605-617 (2001).
87. Kobielak, A. & Fuchs, E. Links between alpha-catenin, NF-kappaB, and squamous cell carcinoma in skin. *Proc Natl Acad Sci U S A* **103**, 2322-2327 (2006).
88. Perez-Moreno, M. & Fuchs, E. Catenins: keeping cells from getting their signals crossed. *Dev Cell* **11**, 601-612 (2006).
89. Martin-Belmonte, F. & Perez-Moreno, M. Epithelial cell polarity, stem cells and cancer. *Nature reviews. Cancer* **12**, 23-38 (2011).
90. Pearson, H.B. *et al.* SCRIB expression is deregulated in human prostate cancer, and its deficiency in mice promotes prostate neoplasia. *J Clin Invest* **121**, 4257-4267 (2011).
91. Zhan, L. *et al.* Deregulation of scribble promotes mammary tumorigenesis and reveals a role for cell polarity in carcinoma. *Cell* **135**, 865-878 (2008).
92. Bilder, D., Li, M. & Perrimon, N. Cooperative regulation of cell polarity and growth by Drosophila tumor suppressors. *Science* **289**, 113-116 (2000).
93. Bilder, D. & Perrimon, N. Localization of apical epithelial determinants by the basolateral PDZ protein Scribble. *Nature* **403**, 676-680 (2000).
94. Cordenonsi, M. *et al.* The Hippo transducer TAZ confers cancer stem cell-related traits on breast cancer cells. *Cell* **147**, 759-772 (2011).
95. Dongre, A. & Weinberg, R.A. New insights into the mechanisms of epithelial-mesenchymal transition and implications for cancer. *Nat Rev Mol Cell Biol* **20**, 69-84 (2019).
96. Greenburg, G. & Hay, E.D. Epithelia suspended in collagen gels can lose polarity and express characteristics of migrating mesenchymal cells. *J Cell Biol* **95**, 333-339 (1982).

97. Ebnet, K. *et al.* The cell polarity protein ASIP/PAR-3 directly associates with junctional adhesion molecule (JAM). *The EMBO journal* **20**, 3738-3748 (2001).
98. Itoh, M. *et al.* Junctional adhesion molecule (JAM) binds to PAR-3: a possible mechanism for the recruitment of PAR-3 to tight junctions. *J Cell Biol* **154**, 491-497 (2001).
99. Feldman, J.L. & Priess, J.R. A role for the centrosome and PAR-3 in the hand-off of MTOC function during epithelial polarization. *Curr Biol* **22**, 575-582 (2012).
100. Wang, Z. *et al.* Binding of PLD2-Generated Phosphatidic Acid to KIF5B Promotes MT1-MMP Surface Trafficking and Lung Metastasis of Mouse Breast Cancer Cells. *Dev Cell* **43**, 186-197 e187 (2017).
101. Marchesin, V. *et al.* ARF6-JIP3/4 regulate endosomal tubules for MT1-MMP exocytosis in cancer invasion. *J Cell Biol* **211**, 339-358 (2015).
102. Yuan, Y. *et al.* Quantitative image analysis of cellular heterogeneity in breast tumors complements genomic profiling. *Science translational medicine* **4**, 157ra143 (2012).
103. Debnath, J., Muthuswamy, S.K. & Brugge, J.S. Morphogenesis and oncogenesis of MCF-10A mammary epithelial acini grown in three-dimensional basement membrane cultures. *Methods* **30**, 256-268 (2003).

Figure Legends

Figure 1. Computational pipeline for the integrative analysis of morphological and molecular data in human breast tumours.

(A) Automated image analysis enables identification of three cell types and quantification of morphological features from an H&E whole tumour section. The distribution of each morphological feature for all cancer nuclei in a tumour image can be summarized using statistical descriptors: median, standard deviation, and skewness. These morphological scores can then represent tumour morphological profiles, which are then associated with genomic aberrations, gene expression data and patient prognosis.

(B) Morphology-Expression hybrid Network representing significant associations between 18 cancer nuclear morphology scores and 1,000 cis-acting genes (feature name sd g.ecc: standard deviation of geometric eccentricity; median m.ecc: median value of moment eccentricity). (C) Illustrative examples of cancer nuclei with high and low value of image moment I1. (D) Illustrative examples of tumours with high and low CNI.

Figure 2. JAM3 as a potential driver of morphological heterogeneity.

(A) Heatmap of RNA expression of genes with highest positive correlation with CNI, samples were annotated with intrinsic subtypes. (B) Boxplot showing the difference in JAM3 gene expression according to JAM3 DNA copy number status. (C) Boxplot showing the difference in JAM3 gene expression according to intrinsic subtypes. (D) Boxplot showing the difference in JAM3 gene expression according to the 10 integrative subtypes. (E) Boxplot showing the difference in JAM3 gene expression according to two main histology subtypes. IDC: Invasive Ductal Carcinoma; ILC: Invasive Lobular Carcinoma. (F) Boxplot showing the difference in JAM3 gene expression according to tumour grades.

Figure 3. JAM-3 regulates nuclear and microtubule organization in epithelial cells.

(A) Control or JAM3-depleted cells were labelled with Hoechst (blue) and immunostained for JAM-3 (green), alpha-tubulin (red) or beta-catenin (green). Scale bars, 20um. (B) Representative images of the 'donut' nuclei (blue; labelled with Hoescht) and the microtubules (red; immunostained with alpha-tubulin) characteristic of MCF10A cells transfected with 2 different siRNAs targeting JAM3. Scale bars, 50um. (C, D) Quantification of perinuclear alpha tubulin intensity (C) and percentage of cells with nuclear donuts (D) in control and JAM-3 depleted cells. Graph shows the representative data of 3 different experiments (n > 12.000 cells). Comparisons among groups were performed by one-way

ANOVA (Newman-Keuls multiple comparison test; *p < 0.05, **p < 0.01, ***p < 0.001, ****p < 0.0001). (E,F) MCF10A cells were allowed to invade "upward" into a Bovine Collagen I matrix, fixed, and labelled with Phalloidin (green) and Hoescht (blue), and then imaged at three different planes. (E) On the left is the invasion index of control and JAM3 depleted MCF10A cells. Representative data from 2 different experiments (n > 5.000 cells). Comparisons among groups were performed by one-way ANOVA (Newman-Keuls multiple comparison test; *p < 0.05, **p < 0.01, ***p < 0.001, ****p < 0.0001). Right shows representative images of cells in the 3 different planes imaged at 0, 30 and 60um. Scale bars, 50um (F) Left panel shows the invasion index of control and JAM3 depleted MCF10A cells treated with DMSO or MMP inhibitor GM6001. Graph shows the data of two different experiments (n > 5.000 cells). Comparisons among groups were performed by one-way ANOVA (Newman-Keuls multiple comparison test; *p < 0.05, **p < 0.01, ***p < 0.001, ****p < 0.0001). Right panel shows representative images of cells in the 3 different invasion planes imaged at 0, 30 and 60um. Scale bars, 50um (G) Heat map showing relative gene expression panel after treating MCF10A cells with 3 different siRNAs targeting JAM3.

Figure 4. JAM3 is required for the morphogenesis of epithelial morphogenesis in 3D. (A,B) MCF10A Control or JAM3-depleted cells by 2 different siRNAs growing in a Matrigel:Collagen thick matrix, allowed to form acini for 2 days, fixed and inmunostained. (A) Maximum projection of representative images of acini labelled with Hoechst (blue) and inmunostained for phalloidin (green), Laminin5 (red) and Fibronectin (white). Scale bars, 50um. (B) Graphs showing the morphology features of the 3 conditions. The majority of the structures formed had 2 or more nuclei, hence considered as Acini. Area was normalized to the Control. F-actin protrusions of the acini were described as Number of neurites and normalized to the control. Fibronectin intensity of the acini was expressed as the mean fibronectin intensity of the whole acini divided by the area of the acini and normalized to the Control. Data shows the result of one experiment where 4 wells per condition were analysed (n > 200 acini per condition). Comparisons among groups were performed by one-way ANOVA (Dunnett´s multiple comparison test) with Prism6 software (*p < 0.05, **p < 0.01, ***p < 0.001, ****p < 0.0001). (C,D) Visual quantification of the number of structures forming normal (round) or abnormal (irregular shape, multiple lobules or protrusive acini) acini at day 8 and expressed as a percentage (n = 100 acini). t student was performed with Prism6 software (*p < 0.05, **p < 0.01, ***p < 0.001, ****p < 0.0001). (D) Confocal sections of Control or JAM3-depleted

MCF10A acini in a Matrigel:Collagen mix, 4 days or 8 days after transfection and labelled with Phalloidin (green), Laminin5 (red) and Hoeschst (blue). Scale bars indicated in the figures.

Figure 5. JAM3 depletion results in nuclear translocation of the YAP and TAZ transcription factors. (A) Quantification of the nuclear:cytoplasmic YAP or TAZ ratios for wild-type and JAM3-depleted cells (n > 15.000 cells). Data shows the results of 3 different experiments. Comparisons among groups were performed by one-way ANOVA (Newman-Keuls multiple comparison test) with Prism6 software (*p < 0.05, **p < 0.01, ***p < 0.001, ****p < 0.0001). (B) Wild-type and JAM3-depleted cells were labelled with Hoechst (blue) and inmunostained for TAZ (green), YAP (red) and alpha tubulin (yellow). Scale bars, 50um. (C) YAP and TAZ nuclear:cytoplasmic ratio as determined by biochemical fractionation in control and siJAM3 depleted (siG RNAi) cells. Results are from one experiment where 1.000.000 cells were lysed per condition. (D) Representative western blots of subcellular fractions for Wild-type and JAM3 depleted cells that were blotted for YAP and TAZ and for several loading controls: KIF5B (cytoskeleton fraction), PCNA and LMNA (soluble nuclear and Chromatin bound fractions) and GAPDH and Beta Tubulin (cytoplasmic and membrane fractions). (E) Relative mRNA levels of CTGF, JAM3, YAP and TAZ normalized to GAPDH for wild-type and JAM3, YAP, or TAZ depleted cells. Mean ± SD (n = 3 replicates/condition).

Figure 6. TAZ is required for EMT in 3D. (A,B) MCF10A Control or JAM3-depleted cells alone or in combination with YAP or TAZ siRNAs were plated in a Matrigel:Collagen thick matrix, allowed to form acini for 2 days, fixed and stained. (A) Maximum projection of representative images of acini labelled with Hoechst (blue) and phalloidin (green). Scale bars, 50um. (B) Graphs showing the morphology features of the 4 conditions. Fibronectin intensity of the acini was expressed as the mean fibronectin intensity of the whole acini divided by the area of the acini and normalized to the Control. F-actin protrusions of the acini were described as Number of neurites per acini and also their length was measured and normalized to the control. Data shows the result of two independent experiments where at least 2 wells per condition were analysed (n > 150 acini per condition). Comparisons among groups were performed by one-way ANOVA (Dunnett´s multiple comparison test) with Prism6 software (*p < 0.05, **p < 0.01, ***p < 0.001, ****p < 0.0001).

Figure 7. Uncoupling the nucleus and microtubules prevents EMT following JAM3 depletion. (A) Percentage of cells with nuclear donuts and (B) quantification of Intensity of perinuclear alpha tubulin in cells treated with JAM3 siRNA alone, or in combination with a panel of siRNAs targeting almost all the LINC components (n > 4.000 cells). Data shows the results of one experiment. Comparisons among groups were performed by one-way ANOVA (Newman-Keuls multiple comparison test) with Prism6 software (*p < 0.05, **p < 0.01, ***p < 0.001, ****p < 0.0001). (C) Representative images of the nuclei (blue, Hoechst) and the MTOC (red, alpha tubulin) of MCF10A cells transfected with a panel of siRNAs targeting several LINC components alone or in combination with JAM3. Scale bars, 50um. (D) Invasion index of MCF10A cells depleted of single genes, or genes in combination. Graphs show the representative data of 2 different experiments (n > 5.000 cells). Comparisons among groups were performed by one-way ANOVA (Newman-Keuls multiple comparison test) with Prism6 software (*p < 0.05, **p < 0.01, ***p < 0.001, ****p < 0.0001). (E) Invasion index of MCF10A cells depleted of single JAM3 and/or SYNE2 into a Collagen matrix. Graph shows the data of one experiment (n > 5.000 cells). Comparisons among groups were performed by one-way ANOVA (Sidak's multiple comparison test) with Prism6 software (*p < 0.05, **p < 0.01, ***p < 0.001, ****p < 0.0001) (F) Relative mRNA levels of CTGF normalized to GAPDH for wild-type, JAM3 depleted, KIF5B+SYNE4 depleted, and Triple knockdown cells. Mean ± SD (n = 3 replicates/condition). (*p < 0.05, **p < 0.01). (G-I) Wild-type, JAM3-depleted cells single or in combination with KIF5B and/or SYNE4 RNAi were labelled with Hoechst (blue) and inmunostained for TAZ (green), YAP (red) and alpha tubulin (yellow). (G) Quantification of the nuclear/cytoplasmic YAP ratio after the RNAi treatments. (H) Quantification of the nuclear/cytoplasmic TAZ ratio after the RNAi treatments. (n>15.000 cells). Data shows the results of 3 different experiments. Comparisons among groups were performed by one-way ANOVA (Newman-Keuls multiple comparison test) with Prism6 software (*p < 0.05, **p < 0.01, ***p < 0.001). (I) Representative images of the wild-type, JAM3 and Triple depleted cells. Scale bars, 50um. (J) YAP and TAZ nuclear:cytoplasmic ratio as determined by biochemical fractionation in wild-type, JAM3 and Triple depleted cells. (K) YAP and TAZ subcellular localization as determined by biochemical fractionation in control, JAM3 depleted, and triple knockdown cells. Pie charts represent the percentage of YAP and TAZ protein localization in each fraction determined by WB of the different extracts for each RNAi treatment. Results are from one experiment where 1.000.000 cells were lysed per condition.

Figure 8. Nuclear morphology defects observed following JAM3 depletion are due to changes in the levels of LMNA and/or LMNB in the nuclear membrane. (A,B) (A) Percentage of cells with nuclear donuts after LMNA or LMNB depletion alone or in combination with JAM-3 (n > 15,000 cells). Data shows the results of 3 different experiments. Comparisons among groups were performed by one-way ANOVA (Newman-Keuls multiple comparison test) with Prism6 software (*p < 0.05, **p < 0.01, ***p < 0.001, ****p < 0.0001). (B) Nuclei of the cells in (A) labelled with Hoechst (blue). Arrows indicate donut nuclei. Scale bars, 50um. (C-E) MCF10A cells treated with different siRNAs and inmunostained with LMNA and LMNB. (C) Panel of images showing the co-staining of LMNA (green) and LMNB (red) after the RNAi treatments. Scale bars, 20 um. (D) Quantification of the LMNA intensity in the Outer nuclear membrane/inner nuclei and normalized to the Control value. (E) Quantification of the LMNB intensity in the Outer nuclear membrane/inner nuclei and normalized to the Control value. (n>15.000 cells). Data shows the results of 2 different experiments. Comparisons among groups were performed by one-way ANOVA (Newman-Keuls multiple comparison test) with Prism6 software (*p < 0.05, **p < 0.01, ***p < 0.001, ****p < 0.0001). (F) LMNA and LMNB intensity levels in the Outer Nuclear membrane of wild-type, JAM3 and Triple depleted cells. Comparisons among groups were performed by one-way ANOVA (Newman-Keuls multiple comparison test) with Prism6 software (*p < 0.05, **p < 0.01, ***p < 0.001, ****p < 0.0001). (G) Cells were depleted of JAM3 alone, or in combination with KIF5B and/or SYNE4, and labelled with Hoechst, LMNA, phospho-LMNA and alpha tubulin. Images (left panel) show cells stained with Hoechst (blue) and immunostained for LMNA (green), phospho-LMNA (red) and alpha tubulin (white). Scale bars, 20um. Graph (right) shows the quantification of the ratio of phosphoLMNA in the inner nuclei or nucleoplasm/ LMNA in the Outer membrane after the RNAi treatments. Graphs shows the representative data of 2 different experiments (n > 5.000 cells). Comparisons among groups were performed by one-way ANOVA (Newman-Keuls multiple comparison test) with Prism6 software (*p < 0.05, **p < 0.01, ***p < 0.001, ****p < 0.0001).

Figure 9. JAM-3 loss drives tumorigenesis and metastasis in breast cancer patients. (A-B) Kaplan-Meier curves illustrating the difference in disease-specific survival over 10 years according to JAM3 gene expression in different subtypes within METABRIC and in Luminal A subtypes of an independent cohort. ILC: Invasive Lobular Carcinoma. Within the luminal A subtype that had large number of samples, patients were spilt into equal-sized groups. For

ILC and the Normal subtype, a best cut-off point was identified by testing different cut-offs. (C) Fold change in frequency of metastasis stratified by JAM3 copy number status. (D) Correlation between KIF5B/SYNE4 expression and JAM3 expression. (E) Boxplots illustrating the difference in JAM3 gene expression according to the copy number status of KIF5B and SYNE4. (F) Kaplan-Meier curves illustrating the difference in disease-specific survival over 10 years according to KIF5B/SYNE4 gene expression in different subtypes within METABRIC.

Figure 10. Model for EMT driven by JAM3 depletion. In wild-type (WT) epithelial cells, the MT are organized such that minus ends are anchored at cell-cell adhesion by JAM3. MT plus ends are anchored at the nuclear membrane by KIF5B-SYNE4 complexes. In this configuration the nucleus is cushioned from deformation, and both YAP and TAZ are deactivated. In JAM3 deficient cells, MTs are reorganized into radial arrays. This confirmation results in nuclear deformation by the MTs, loss of LMNA from the membrane, increased LMNA phosphorylation, “softening” of the nucleus, translocation of YAP and TAZ into the nucleus, and upregulation of EMT genes.

Figure S1. On-target effects of JAM3 siRNA.

(A) JAM3 mRNA levels as determined by qRT-PCR following depletion by single or pooled siRNAs. Data was normalized to GAPDH mRNA and control (wild type). Mean +/- SD (n= 4 wells/condition). (B) Detection of JAM3 protein by Western blotting of lysates made from cells transfected with either siGenome (siG) or On Target plus pools targeting JAM3. (C) Percentage of cells with nuclear donuts in Control and JAM-3 depleted cells by using single and pooled siRNAs targeting Jam3. Both graphs show a single experiment (n > 4.000 cells). Comparisons among groups were performed by one-way ANOVA (Newman-Keuls multiple comparison test) with Prism6 software (*p < 0.05, **p < 0.01, ***p < 0.001, ****p < 0.0001). (D) Percentage of cells with donut shape in Control or JAM3 depleted hTERT1 RPE-1 cells. Data shows the results of 2 different experiments (n > 7.000 cells). t student was performed with Prism6 software (***p < 0.001). (E) Representative images of the nuclei (blue, Hoechst) and microtubules (red, alpha tubulin) in Control and JAM-3 depleted hTERT1 RPE-1 cells. Scale bars, 50um. (F) Representative images of the nuclei (blue, Hoechst) and phalloidin (green, actin) of MCF10A cells mock transfected or transfected with JAM3 RNAi. Scale bars, 50um. (G) Quantification of the total actin intensity in the nuclear area and the texture of the actin fibers in the whole cell area in MCF10A cells mock transfected and JAM3 depleted. Graphs show the data of one experiment (n > 5.000 cells). t student was performed with Prism6 software. (H) Confirmation of gene expression with individual primers. Relative mRNA levels of Microtubule Associated Protein 1B (MAP1B), Transcription factors such as FOXC2

or the ZEB2 and genes related to ECM organization such as Fibronectin 1 (FN1), Integrin Subunit Alpha 5 (ITGA5), Stromelysin 1 (MMP3) or Procollagen C-Endopeptidase (BMP1) were normalized to GAPDH for wild-type and JAM3 depleted cells. Mean ± SD (n = 4 replicates/condition). (⁎p < 0.05, ⁎⁎p < 0.01).

Figure S2. Nuclear deformation and microtubule reorganization are hallmarks of EMT. (A-C) MCF10A cells mock transfected or transfected with JAM3 RNAi and treated with DMSO or TGF beta for 48 hours. (A) Percentage of cells with "Low Nuclear Roundness" and (B) EB1 distribution was quantified by the Radial Mean Intensity in the whole cell and normalized to the Control value. (n > 1,000 cells). Data shows the result of one experiment. Comparisons among groups were performed by one-way ANOVA (Sidak's multiple comparison test) with Prism6 software (⁎p < 0.05, ⁎⁎p < 0.01, ⁎⁎⁎p < 0.001, ⁎⁎⁎⁎p < 0.0001). (C) Representative images of the nuclei (blue) and the EB1 (green). Scale bars, 50 μm.

Figure S3. JAM3 depletion affects acini morphogenesis.
Time frames of a time-lapse movie showing the normal round acini of mock transfected acini in contrast to the invasive acini after JAM3 depletion. Acini were imaged by using the Brightfield and frames were taken each 10 minutes for 2 days.

Figure S4. Specific effects of JAM3 depletion of YAP and TAZ nuclear translocation. (A) Quantification of the nuclear:cytoplasmic YAP ratios and total YAP intensity (whole cell) and (B) TAZ nuclear:cytoplasmic ratios and total TAZ intensity (whole cell) in Wild-type, YAP, TAZ and (YAP+TAZ) MCF10A depleted cells using antibodies specific for YAP and TAZ (n > 15.000 cells). Data shows the results of 3 different experiments. Comparisons among groups were performed by one-way ANOVA (Newman-Keuls multiple comparison test) with Prism6 software (⁎p < 0.05, ⁎⁎p < 0.01, ⁎⁎⁎p < 0.001, ⁎⁎⁎⁎p < 0.0001). (C) Representative images of Wild-type cells, treated with RNAi targeting YAP, TAZ or (YAP+TAZ) or seeded at high or low density and co-stained with TAZ (green) and YAP (red). Scale bars, 50um.

Figure S5. YAP and TAZ activation results in remodelling of the ECM following JAM3 depletion. (A) Number of Collagen I spots per area of the cell in Wild-type, JAM3, YAP and/or TAZ depleted cells single or in combination with JAM3 RNAi. (n > 5.000 cells). Data shows the results of 2 different experiments. Comparisons among groups were performed by one-way ANOVA (Newman-Keuls multiple comparison test) with Prism6 software (⁎p < 0.05, ⁎⁎p

< 0.01, ***p < 0.001, ****p < 0.0001). Images showing the Hoechst (blue) and Collagen I (red) immunostaining of Wild-type and JAM3 depleted cells (vesicles). Scale bars, 20um. (B) Quantification of the Soluble Fibronectin in the extracellular space normalized to its area of Wild-type, JAM3, YAP and/or TAZ depleted cells single or in combination with JAM3 RNAi. (n>15.000 cells). Data shows the results of 2 different experiments. Comparisons among groups were performed by one-way ANOVA (Newman-Keuls multiple comparison test) with Prism6 software (*p < 0.05, **p < 0.01, ***p < 0.001). Images shows the cells labelled with Hoechst (blue) and Phalloidin (red) and inmunostained with Fibronectin (green) w/o permeabilization. Scale bars, 50um.

Figure S6. JAM3 regulates LMNA and LMNB protein localization and levels. (A) Quantification of the total nuclear levels (Inner nuclear intensity + Outer nuclear Intensity) of either LMNA or LMNB in control MCF10A cells, or following depletion of LMNA or LMNB. Data shows the results of 3 different experiments (n > 15.000 cells). Comparisons among groups were performed by one-way ANOVA (Newman-Keuls multiple comparison test) with Prism6 software (*p < 0.05, **p < 0.01, ***p < 0.001, ****p < 0.0001). (B) Representative images of Wild-type cells, treated with LMNA RNAi or LMNB RNAi and immunostained with LMNA antibody (green) or two different LMNB antibodies (red). Scale bars, 20um. (C) Total mRNA levels of LMNA and LMNB normalized to GAPDH for wild-type following single, double, or triple gene depletion, or (D) ratio of LMNA:LMNB mRNA following single, double, or triple gene depletion. Mean ± SD (n = 3 replicates/condition). (*p < 0.05, **p < 0.01). (E,F) Total levels of LMNA and LMNB by co-immunostaining after several RNAi treatments. (E) Quantification of the LMNA intensity in the Outer nuclear membrane plus the intensity in the inner nuclei and normalized to the Control value. (F) Quantification of the LMNB intensity in the Outer nuclear membrane plus the intensity in the inner nuclei and normalized to the Control value. Data shows the results of 3 different experiments (n>15.000 cells). Comparisons among groups were performed by one-way ANOVA (Newman-Keuls multiple comparison test) with Prism6 software (*p < 0.05, **p < 0.01, ***p < 0.001, ****p < 0.0001). (G,H) Quantification of the nuclear/cytoplasmic YAP ratio and TAZ ratio after the LMNA RNAi treatments. (G) Quantification of the nuclear/cytoplasmic TAZ ratio after the RNAi treatments. (n > 15.000 cells). Data shows the results of 3 different experiments. Comparisons among groups were performed by one-way ANOVA (Newman-Keuls multiple comparison test) with Prism6 software (*p < 0.05, **p < 0.01, ***p < 0.001, ****p < 0.0001).

(I) Invasion of Wild-type, JAM3, LMNA and LMNB depleted cells single or in combination with JAM3 RNAi. Graph shows the representative data of 2 different experiments (n > 5.000 cells). Comparisons among groups were performed by one-way ANOVA (Newman-Keuls multiple comparison test) with Prism6 software (*p < 0.05, **p < 0.01, ***p < 0.001, ****p < 0.0001).

Figure S7. **Chemical inhibition of Kinesin-1 mirrors the effects of KIF5B RNAi.** (A-C) MCF10A cells mock transfected, transfected with JAM3 RNAi single or in combination with SYNE4 RNAi and treated with DMSO or RBL at the indicated concentrations for 48 hours. (A) Percentage of cells with nuclear donuts and (B) Quantification of the LMNA intensity in the Outer nuclear membrane/inner nuclei and normalized to the Control value. (n > 3.000 cells). Comparisons among groups were performed by one-way ANOVA (Newman-Keuls multiple comparison test) with Prism6 software (*p < 0.05, **p < 0.01, ***p < 0.001, ****p < 0.0001). (C) Representative images of the nuclei (blue) and the Lamin A (green) of all the conditions. Scale bars, 20um.

Figure S8. JAM3 depletion does not affect cell cycle progression. (A) Cell cycle profiles of MCF10A cells wild-type or treated with different RNAi. 48h after transfection, cells were fixed, stained with propidium iodide, and analyzed of cell cycle progression by flow cytometry. Data was plotted as a 3D histogram and the table shows the percentage of cells in each cell cycle phase. Data derived from two different experiments. (n = 20.000 gated cells per condition). (B) Mitotic index quantification of MCF10A cells wild-type or treated with different RNAi single and/or in combination with JAM3 RNAi for 48h. Cells were fixed, labelled with Hoechst and imaged on a confocal microscope. Then cells were segmented on the Hoechst channel and classified by their nuclear intensity and nuclei size. Graphs shows the representative data of 3 different experiments (n > 15.000 cells). Comparisons among groups were performed by one-way ANOVA (Newman-Keuls multiple comparison test) with Prism6 software (*p < 0.05, **p < 0.01, ***p < 0.001, ****p < 0.0001). (C) Representative images of JAM3-depleted cells showing both mitotic and interphase cells. Cells were labelled with Hoechst (blue) and inmunostained for alpha tubulin (red). Scale bars, 20um. (D,E) Immunofluorescence staining against phosphorylated histone H2AX for wild-type or treated with different RNAi single and/or in combination with JAM3 RNAi for 48h. (D) Quantification of gammaH2AX nuclear intensity normalized to the wild type cells. Data shows the results of 2 different experiments. (n > 8.000 cells). Comparisons among groups were performed by one-way ANOVA (Newman-Keuls multiple comparison test) with Prism6 software (*p <

0.05, **p < 0.01, ***p < 0.001, ****p < 0.0001). (E) Examples of representative images for control cells, JAM3, and p53 depleted cells labelled with Hoechst (blue) and gammaH2AX (green). Scale bars, 50um.

Figure S9. Related to Methods and the Automated analysis in 2D. (A-O) Automated segmentation for feature extraction in 2D cultures. (A) Whole Nuclei segmented on Hoechst (DNA) channel. (B) Ring region of the Inner nuclei selected and considerer as ´nuclei´ for all the analysis in 2D. (C) Perinuclear ring region used as 'cytoplasm' for all the analysis. Cell cores segmented usually on (D) alpha Tubulin (microtubules) channel. Cell boundaries were divided into (E) free edges (solid lines) and cell-cell borders (F) (dotted lines) to determine Neighbour Fraction (NF). (G) Mitotic cells were classified using the Inner nuclei Hoechst intensity and excluded from all the analysis except for the Mitotic Index. (H) Cells in contact with the border edges were removed and excluded from all the analysis. (I) Detected donut nuclei by Acapella software based on a thresmask for Hoechst. Scale bars, 50 μm. (J) For the Lamin analysis whole Nuclei was segmented on Hoechst (DNA) channel at 40x or 60x. (K) Ring region of the Outer nuclei selected for the Lamin analysis. (L) Ring region of the Inner nuclei selected and considerer as ´nuclei´ for all the Lamin analysis. Scale bars, 20 μm. (M) Actin (F-actin) channel was used to segment the cell cores (only for Soluble Fibronectin analysis). (N) Fibronectin detected in the area outside the colony. Scale bars, 50 μm. (O) Automated segmentation of Collagen vesicles using a spot finding algorithm. Scale bars, 20 μm. (P,Q) Plots showing the Linear Regression analysis performed to correct YAP and TAZ ratios by cell number (in this case only TAZ examples are shown). (P) TAZ ratio Observed by cell number of mock-transfected cells and cells transfected with JAM3 or Triple siRNA. (Q) TAZ ratio (Observed-Predicted) of the above conditions after the cell number correction.

Figure S10. Related to Methods and the Automated analysis in 3D and Bottom to top invasion assays. (A) Automated segmentation for feature extraction from images of organotypic cultures. (I) Total number of structures (single cells or group of cells) was detected by the colonies module according to the Actin channel. (II) Whole Nuclei segmented on Hoechst (DNA) channel per structure. Nuclei without actin in the perinuclear area were excluded from all the analysis. (III) Number of cells per acini was defined by using a Linear Classifier filter according to the number of nuclei per structure (one nuclei per structure = single cell; two or more nuclei per structure = colony consider as real acini). (IV) Automated segmentation of spikes using a Neurites finding algorithm. Scale bars, 50 μm. (B) Automated segmentation for Invasion quantification in a Bovine collagen matrix. (I) Whole Nuclei

segmented on Hoechst (DNA) channel in every plane. A nuclei contrast threshold was chosen for every experiment to select only cells that were really in the plane selected and therefore avoiding to quantify the same cell in several planes. Left pic, bottom plane. Right pic, middle plane. (II) Second step segmentation on the cell cores based on the Actin (F-actin) channel. Nuclei without actin in the perinuclear area were excluded from all the analysis. Left pic, bottom plane. Right pic, middle plane. Scale bars, 50 μm.

Supplemental Table S1: Nuclear shape feature names and definitions.

Feature	**Definition**
Acircularity	Fraction of pixels outside of a circle with same size
Shape factor	Ratio of largest and smallest diameter
I1	1st Hu's invariant moment
I2	2nd Hu's invariant moment
Geometric eccentricity	Eccentricity based on geometric information
Moment eccentricity	Eccentricity based on image moments

Supplemental Table S2: Top 30 genes with the strongest correlation (positive or negative) between their gene expression and CNI.

Symbol	Cytoband	description	cor	cor.qval
JAM3	**11q25d**	**Junctional adhesion molecule 3**	**0.374140674**	**2.93E-06**
DACT3	19q13.32b	dapper, antagonist of beta-catenin, homolog 3	0.360405303	5.26E-06
PODN	1p32.3c	podocan	0.35857884	5.46E-06
ZCCHC24	10q22.3e	zinc finger, CCHC domain containing 24	0.35566043	5.73E-06
MSRB3	12q14.3a	methionine sulfoxide reductase B3	0.354708698	5.80E-06
PLAC9	10q22.3f	placenta-specific 9	0.34914394	9.06E-06
FBLN1	22q13.31c	fibulin 1	0.341533656	1.64E-05
MYH11	16p13.11a	myosin, heavy chain 11, smooth muscle	0.340572284	1.75E-05
SPARCL1	4q22.1a		0.335462425	2.39E-05
PDGFRL	8p22b	platelet-derived growth factor receptor-like	0.332219695	2.80E-05
PGM5	9q13a-b		0.331297275	2.91E-05
PRKD1	14q12d	protein kinase D1	0.329774726	3.09E-05
SGOL1	3p24.3b	shugoshin-like 1 (S. pombe)	-0.329650763	3.10E-05
SPARCL1	4q22.1a	SPARC-like 1 (hevin)	0.3289817	3.18E-05
NDN	15q11.2d	necdin homolog (mouse)	0.328428741	3.24E-05
CLDN5	22q11.21c	claudin 5	0.327973114	3.29E-05
PLSCR4	3q24c-d	phospholipid scramblase 4	0.327146182	3.37E-05
UBE2S		ubiquitin-conjugating enzyme E2S	-0.326531157	3.43E-05

PGM5	9q13a-b	phosphoglucomutase 5	0.325278498	3.57E-05
OLFML1	11p15.4b	olfactomedin-like 1	0.324747094	3.63E-05
KIF11	10q23.33a	kinesin family member 11	-0.32441562	3.66E-05
UBE2C	20q13.12b	ubiquitin-conjugating enzyme E2C	-0.323362505	3.80E-05
UBE2C	20q13.12b		-0.322898827	3.86E-05
BC036512	12p13.31d		-0.321418993	4.05E-05
PKMYT1	16p13.3d	protein kinase, membrane associated tyrosine/threonine 1	-0.320962094	4.10E-05
CEP55	10q23.33b	centrosomal protein 55kDa	-0.320803389	4.12E-05
CCDC80	3q13.2a	coiled-coil domain containing 80	0.318581494	4.37E-05
TSHZ2	20q13.2b	teashirt zinc finger homeobox 2	0.31853181	4.37E-05
CCNA2	4q27c	cyclin A2	-0.318419623	4.38E-05
SLIT2	4p15.31d	slit homolog 2 (Drosophila)	0.318328789	4.39E-05

Supplemental Table S3 : List of cell culture resources used in this study

Supplemental Table S4: Antibodies used in this study

Supplemental Table S5: siRNAs used in this study

Supplemental Table S6: qRT-PCR primers used in this study

Supplemental Table S7: Software used in this study

Figure 1. Arias-Garcia et al.

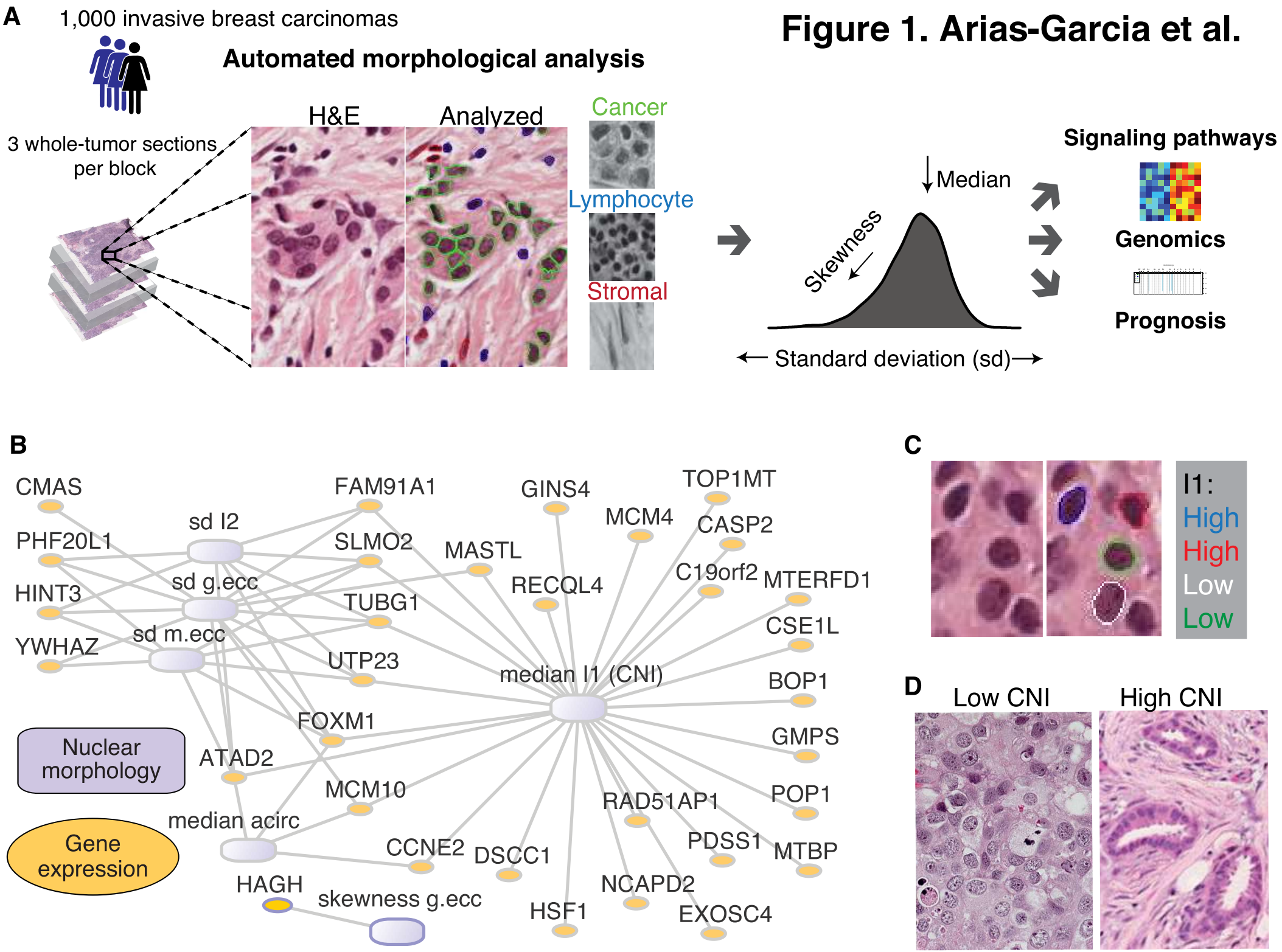

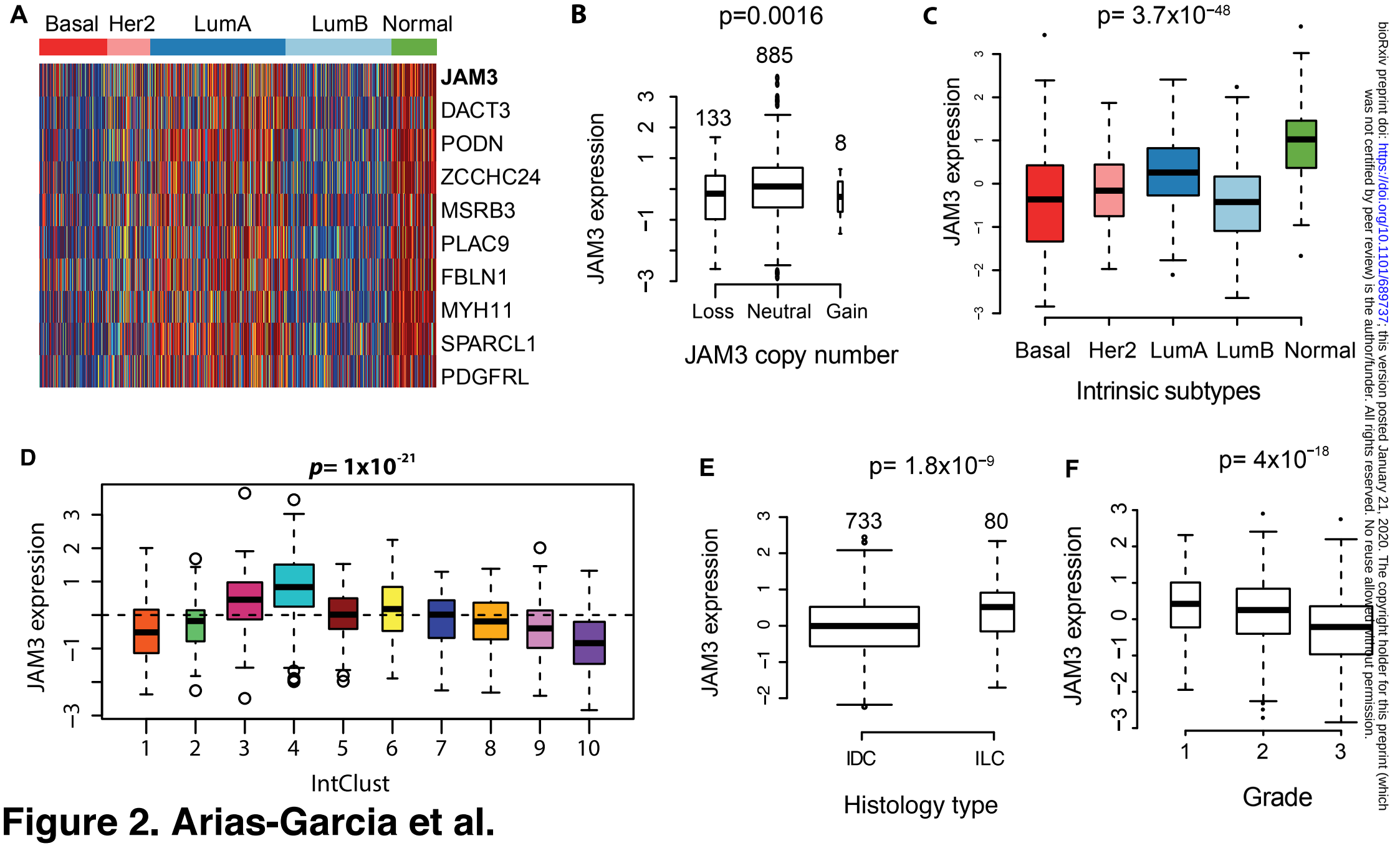

Figure 2. Arias-Garcia et al.

Figure 3. Arias-Garcia et al.

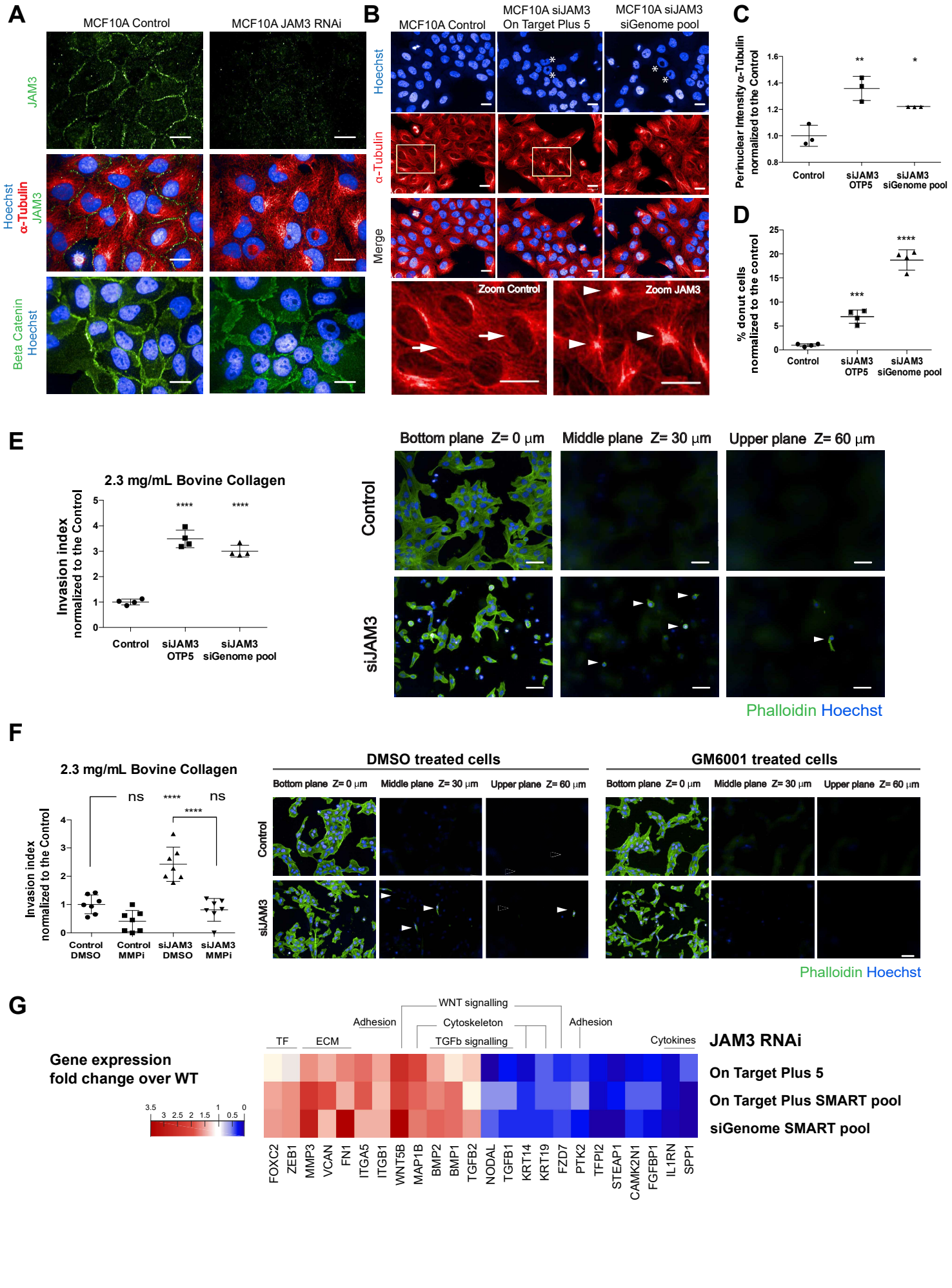

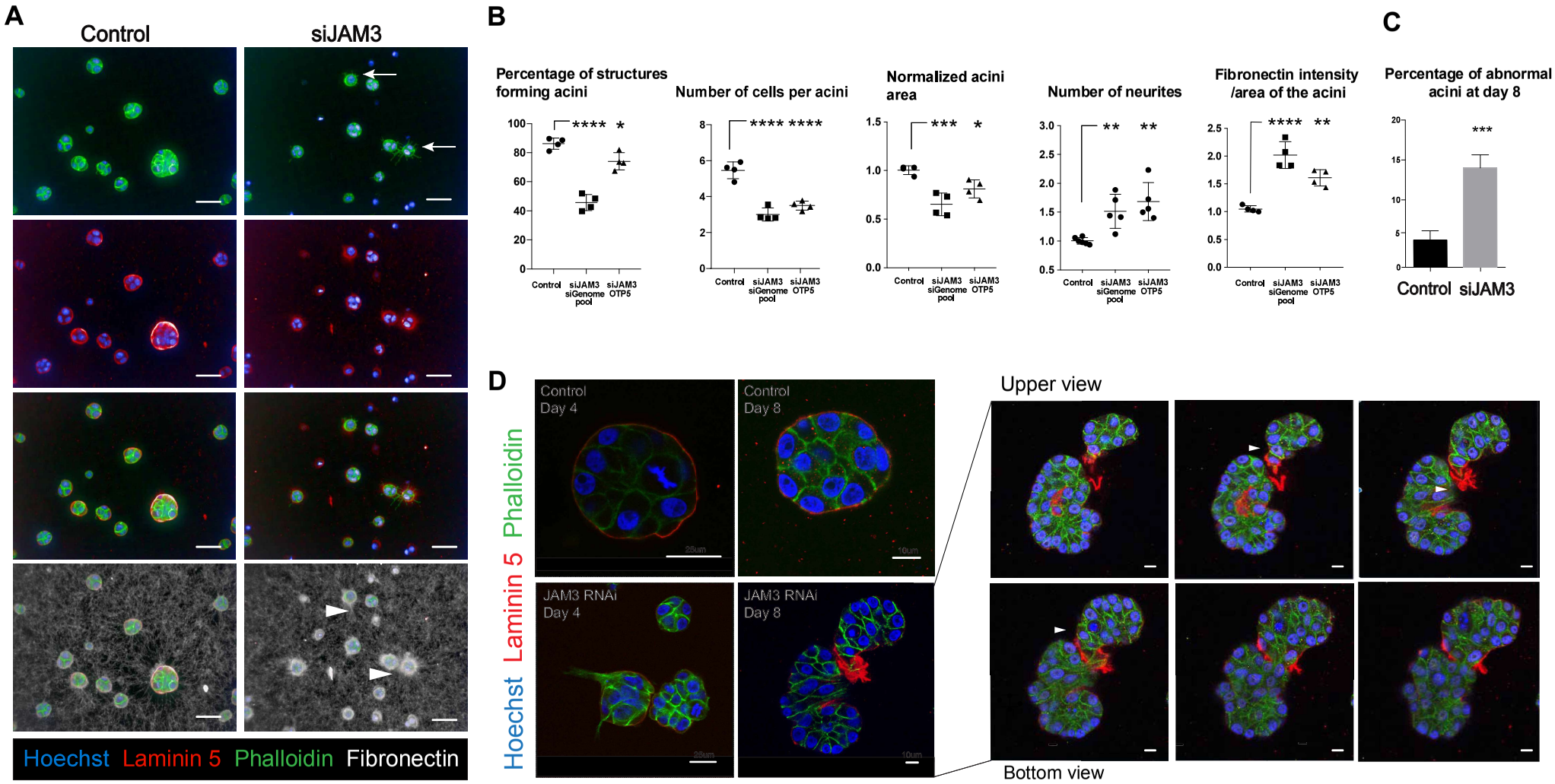

Figure 4. Arias-Garcia et al.

Figure 5. Arias-Garcia et al.

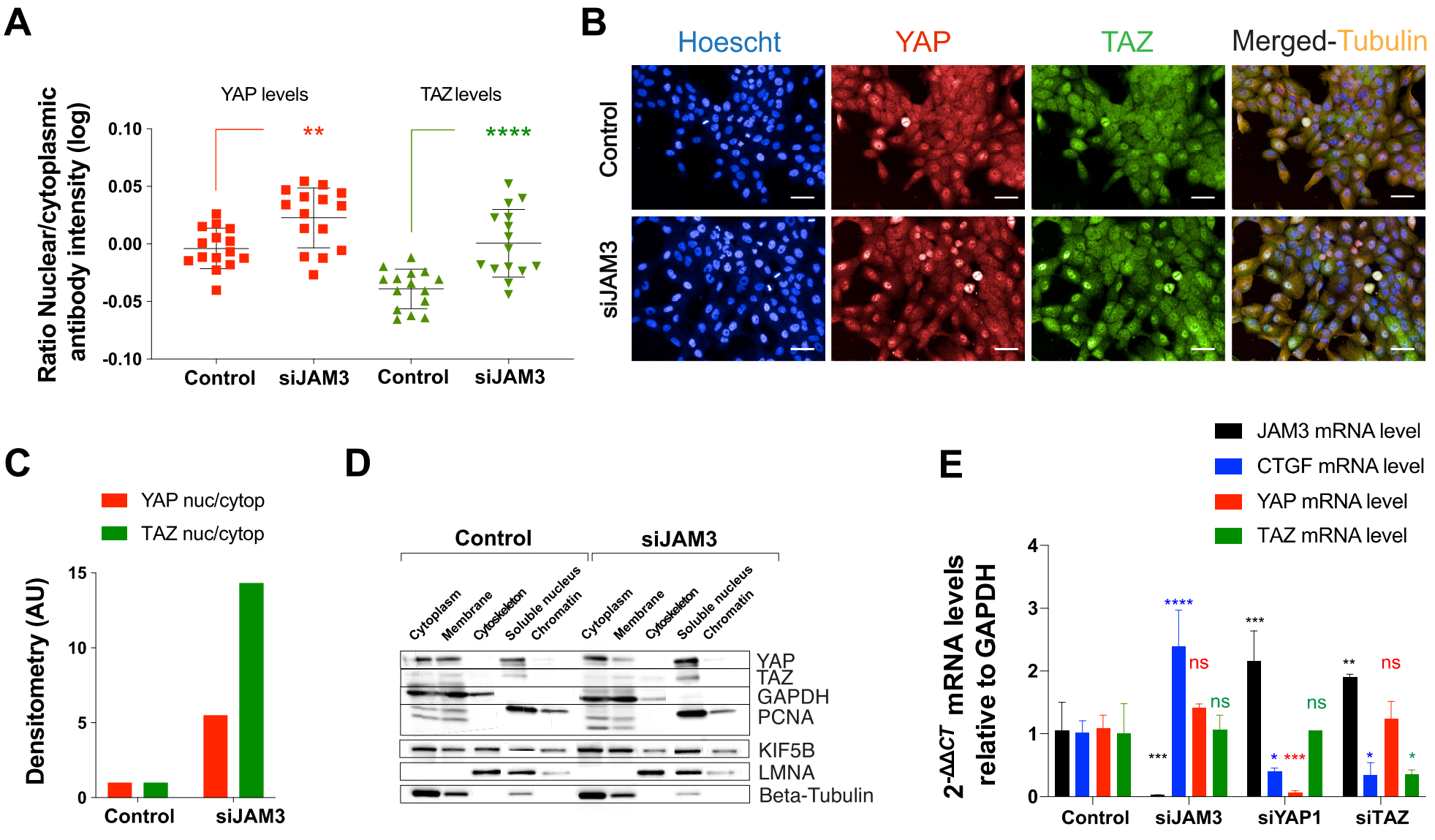

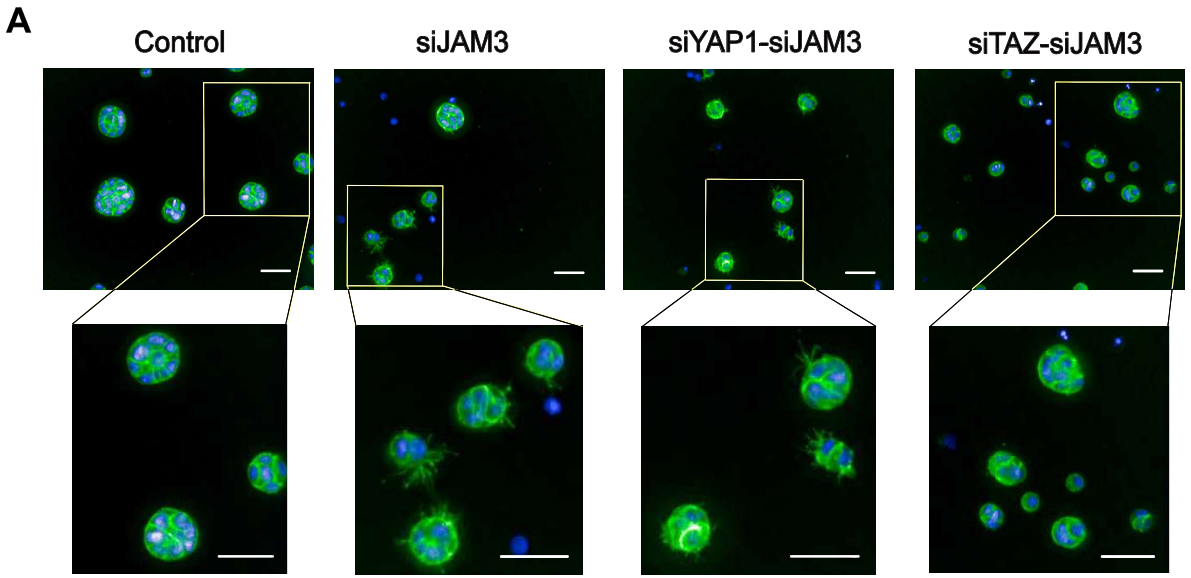

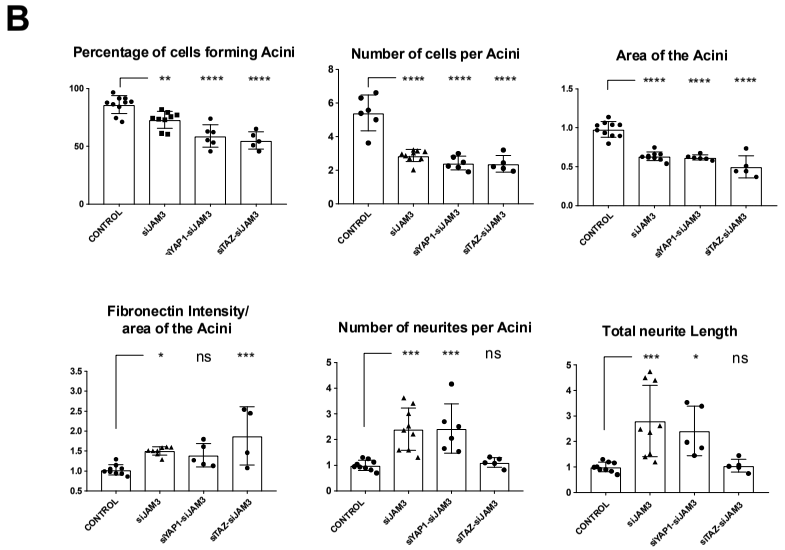

Figure 6. Arias-Garcia et al.

Figure 7. Arias-Garcia et al.

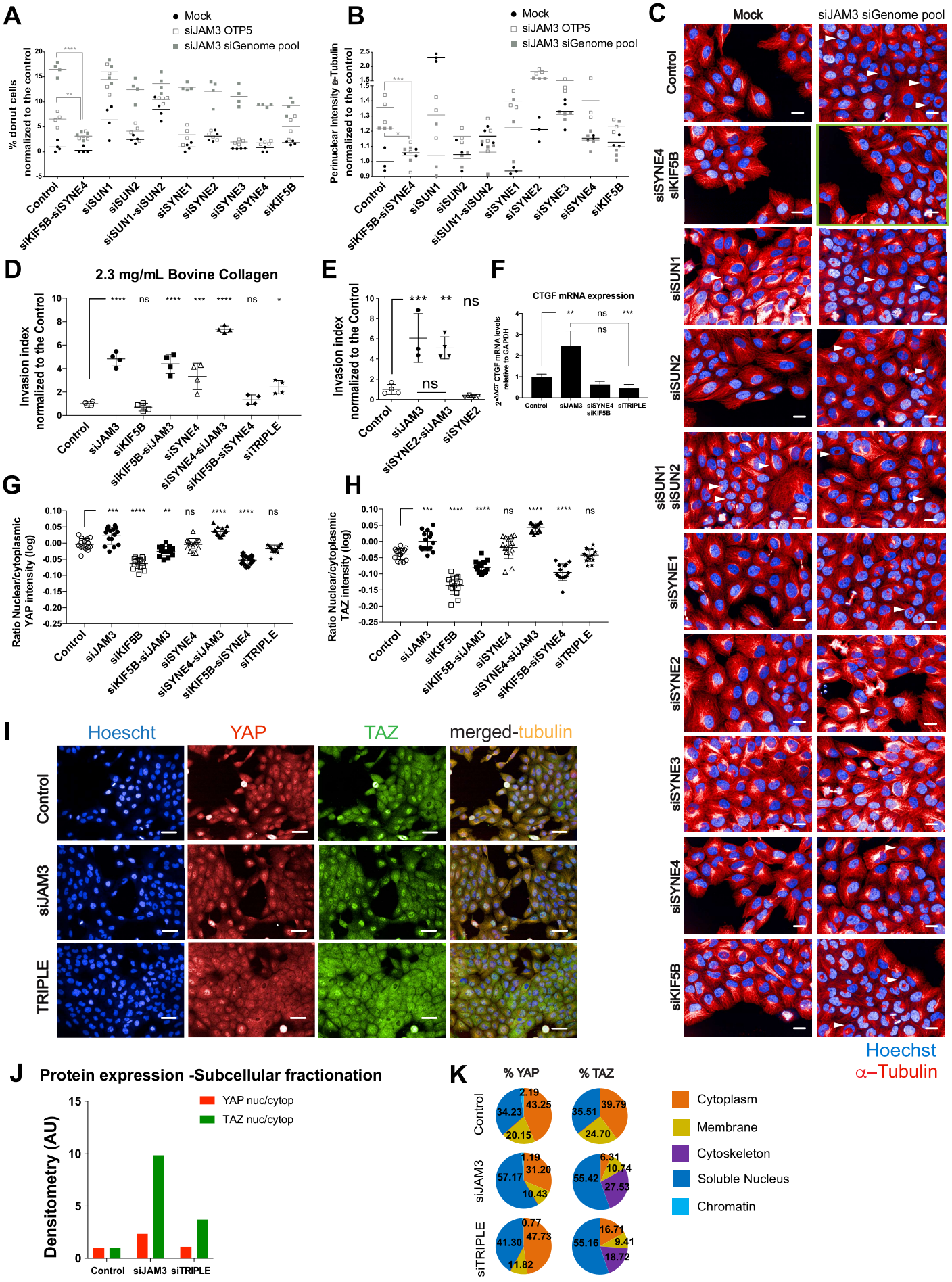

Figure 8. Arias-Garcia et al.

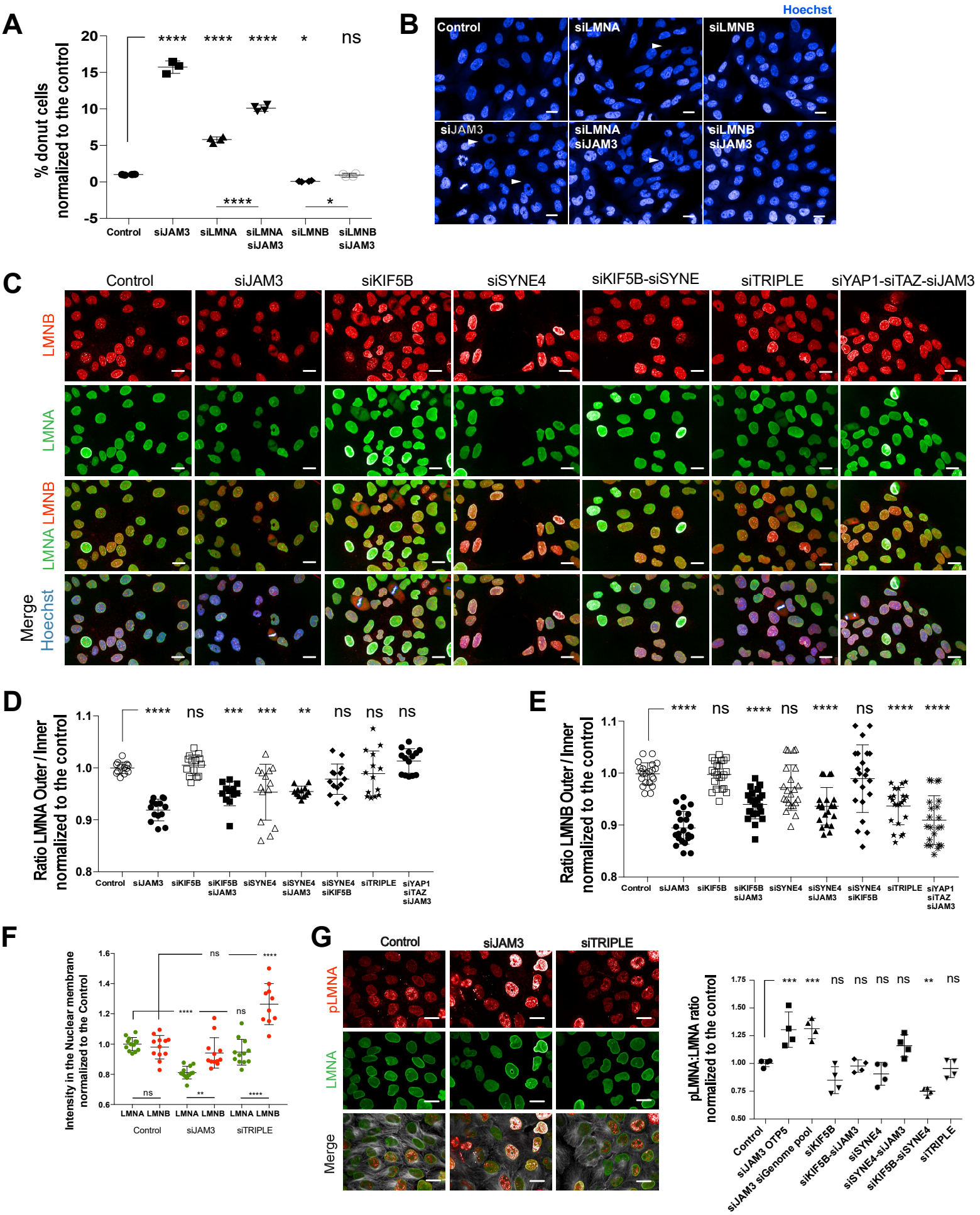

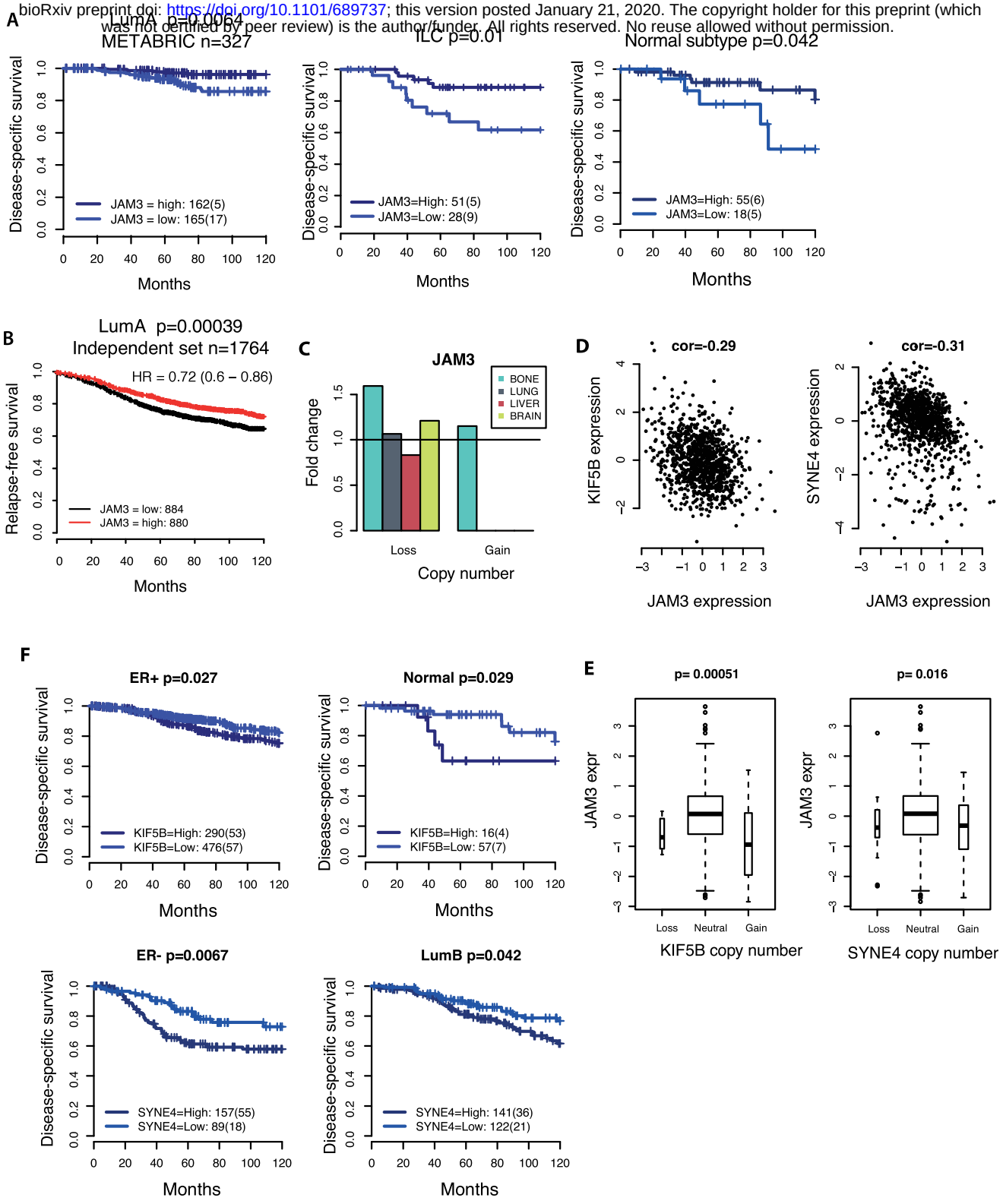

Figure 9. Arias-Garcia et al.

Figure 10. Arias-Garcia et al.